

Turbulence and energy budget in a self-preserving round jet: direct evaluation using large eddy simulation

C. BOGEY¹† AND C. BAILLY^{1,2}

¹Laboratoire de Mécanique des Fluides et d'Acoustique, UMR CNRS 5509,
Ecole Centrale de Lyon, 69134 Ecully Cedex, France

²Institut Universitaire de France, 103 Boulevard Saint-Michel, 75005 Paris, France

(Received 6 February 2008 and in revised form 5 January 2009)

An axisymmetric jet at a diameter-based Reynolds number of 1.1×10^4 is computed by a large eddy simulation (LES) in order to investigate its self-similarity region. The LES combines low-dissipation numerical schemes and explicit filtering of the flow variables to relax energy through the smaller scales discretized. The computational domain extends up to 150 jet radii in the downstream direction, which is found to be large enough to discretize a part of this region. Turbulence in the self-preserving jet is characterized by evaluating explicitly from the LES fields the second- and third-order moments of velocity, the pressure–velocity correlations as well as the budgets for the turbulent kinetic energy and for its components. Reference solutions are thus obtained. They agree well with the experimental data given by Panchapakesan & Lumley (*J. Fluid Mech.*, vol. 246, 1963, p. 197) for a jet at the same Reynolds number. The distance required to achieve self-similarity in the LES, around 120 radii from the inflow, is particularly similar to that in the experiment. The discrepancies observed with respect to the data provided by Panchapakesan & Lumley and by Hussein, Capp & George (*J. Fluid Mech.*, vol. 258, 1994, p. 31) for a jet at a higher Reynolds number, specially regarding the turbulence diffusion and the dissipation, are discussed. They appear largely resulting from the approximations made in the experiments to estimate the quantities that cannot be measured with accuracy. The role of the pressure terms in the energy redistribution is also clarified by the LES. Moreover, the turbulent energy budget is calculated in the jet from an equation derived from the filtered compressible Navier–Stokes equations, which includes the dissipation due to the explicit filtering. This has allowed us to assess the behaviour of the LES approach based on relaxation filtering (LES-RF) from the contributions of filtering and viscosity to energy dissipation. The filtering activity is particularly shown to adjust by itself to the grid and flow properties.

1. Introduction

The turbulent round jet is a model flow that has been investigated experimentally extensively over the last 50 years. Two flow regions have been distinguished: the flow-establishment region and, farther in the downstream direction, the self-preservation or self-similarity region where the flow profiles across the jet are self-similar. During the

† Email address for correspondence: christophe.bogey@ec-lyon.fr

sixties, some researchers including Davies, Fisher & Barratt (1962), Sami, Carmody & Rouse (1967) and Sami (1967) studied turbulence in the first jet region. Wygnanski & Fiedler (1969) also made some measurements of flow quantities in the self-similarity region of a jet at Reynolds number $Re_D = u_j D / \nu = 10^5$, where u_j is the jet nozzle exit velocity, D the diameter and ν the molecular viscosity. The self-preservation region was attained at 70 diameters downstream of the jet nozzle and is characterized by the linear increase of u_j / u_c , where u_c is the centreline mean axial velocity, and by constant turbulence intensities along the jet axis. In this jet region, the mass flow rate was moreover found by Ricou & Spalding (1961) to grow linearly, and two-point statistics were recently described by Burattini, Antonia & Danaila (2005). In the early nineties, the solutions of Wygnanski & Fiedler (1969) were complemented by the experimental data obtained by Panchapakesan & Lumley (1993) and by Hussein, Capp & George (1994) in self-preserving jets, respectively, at Reynolds numbers $Re_D = 1.1 \times 10^4$ and $Re_D = 10^5$. Careful measurements of the second- and third-order velocity moments were especially provided and were used to evaluate the budget for the turbulent kinetic energy.

The determination of the turbulent energy budget in jets, however, remains difficult due to differences and uncertainties in the experimental techniques. In addition, some turbulent quantities involved in the budget, such as the pressure–velocity correlations, cannot be easily measured, which has led to the use of different approximations and modellings for the estimation of the energy terms. In the energy budgets calculated by Sami (1967) and by Weisgraber & Liepmann (1998) in the flow-establishment region of round jets, the pressure-transport terms were for instance obtained by difference by the former and simply neglected by the latter. In the same way, energy dissipation cannot be usually evaluated directly and must be inferred from turbulence considerations. Expressions assuming isotropic or semi-isotropic turbulence were consequently used for calculating dissipation in planar and round turbulent jets by Bradbury (1965), Gutmark & Wygnanski (1976) and Wygnanski & Fiedler (1969). Relations for axisymmetric turbulence were also derived later by George & Hussein (1991). In the particular works of Panchapakesan & Lumley (1993) and Hussein *et al.* (1994), different processes were applied for the computation of the energy terms in the self-preserving circular jets: Panchapakesan & Lumley removed the pressure diffusion in the energy budget and obtained the dissipation as the closing balance, whereas Hussein *et al.* estimated the energy dissipation from measurements using the assumption of local axisymmetry of small scales, and then evaluated the pressure diffusion as the remaining term. This resulted in serious discrepancies between the solutions, the pressure diffusion neglected by Panchapakesan & Lumley being for example significant in the energy budget of Hussein *et al.*

Given the experimental weaknesses, numerical simulations may be an appropriate way to describe exhaustively the turbulence developing in jets, because theoretically they give access to all flow quantities. The limitations are then due to the computational resources, and errors might originate from the numerical methods and turbulence modellings. Direct numerical simulation (DNS) can be used for flows at low Reynolds numbers, as successfully shown for instance by Mansour, Kim & Moin (1988) for a turbulent channel flow, and by Boersma, Brethouwer & Nieuwstadt (1998) and Stanley, Sarkar & Mellado (2002) for round and planar jets. However, for flows at higher Reynolds numbers, which are typically dealt with in experiments, large eddy simulation (LES) must be performed. In LES, as reported in detail in the books of Geurts (2004) and Sagaut (2005), the complexity of turbulent flows is reduced by applying a low-pass filtering to the Navier–Stokes equations. The filter

width is usually taken as the mesh size so that in practice one aims at providing solutions for the scales larger than the grid spacing, whereas the smaller scales are removed. Jets have been recently examined in this way. Among other studies, Dejoan & Leschziner (2005) computed the energy budget in a plane turbulent wall jet, and Uddin & Pollard (2007) discussed the existence of the virtual origin of round jets. Bogey & Bailly (2006a,c, 2007) and Berland, Bogey & Bailly (2007) also investigated the initial flow development and noise generation in subsonic and supersonic jets.

LES is a powerful method, but there must be a constant care to ensure that the solutions obtained for turbulent flows are physically correct. Energy dissipation is in particular a key point to consider, because an artificial dissipation is required to regularize the flow. The various subgrid-scale (SGS) models that have been proposed to reproduce the effects of the SGS terms generated by the filtering of the flow equations have, for instance, difficulty in accounting for the SGS dissipation, which might be under- or overestimated as noted by Vreman, Geurts & Kuerten (1997) and by Le Ribault, Sarkar & Stanley (1999). Among the SGS models, eddy viscosity models are widely used, but they might be inappropriate as pointed out by Domaradzki & Yee (2000) and by Bogey & Bailly (2005a,b) because eddy viscosity is similar to molecular viscosity. This observation has led to SGS models involving higher order viscosities, such as hyperviscosity in Dantinne *et al.* (1998) or spectral vanishing viscosity in Pasquetti (2006), designed to be active mainly in the high-frequency range. Another LES approach consists in employing the numerical dissipation of discretization schemes as an implicit SGS model (see e.g. Grinstein & Fureby 2002). This approach is often referred to as implicit LES (ILES), because an explicit calculation of the SGS terms is unnecessary. The reliability of an ILES depends however on the numerical schemes, whose dissipation has to be characterized in terms of magnitude and spectral properties. Garnier *et al.* (1999) obtained, for example, excessive damping using shock-capturing schemes, while Domaradzki, Xiao & Smolarkiewicz (2003) showed that it is possible to estimate the effective eddy viscosity acting in an ILES. A method has also been proposed recently by Hickel, Adams & Domaradzki (2006) to match the numerical viscosity of ILES schemes with theoretical viscosity for isotropic turbulence.

Following the basic ILES idea of dissipating energy through a numerical SGS functional model, an LES method combining low-dissipation schemes and a high-order/selective filtering of the flow variables has been developed, specially by Stolz, Adams & Kleiser (2001), Rizzetta, Visbal & Blaisdell (2003), Mathew *et al.* (2003) and Bogey & Bailly (2006c). Mathew *et al.* (2003), in particular, derived an explicit filtering of the variables from the deconvolution model of Stolz *et al.* (2001). To extend the terminology of the latter authors, the present methodology is defined here as LES based on relaxation filtering (LES-RF), because the filtering aims at diffusing energy through the smaller scales discretized. In practice the filtering can be performed explicitly or implicitly by adding terms into the flow equations. Works are still on to study the LES-RF method. They resort naturally to the quantification of subgrid dissipation in energy budgets, as it has been performed in channel flows by Schlatter, Stolz & Kleiser (2006) and in round jets by Bogey & Bailly (2006c).

In the present study, a circular jet at a Mach number $M = u_j/c_0 = 0.9$, where c_0 is the sound speed in the ambient medium, and at a Reynolds number $Re_D = 1.1 \times 10^4$ is simulated by the LES-RF method. The LES is performed using space and time discretization schemes with low dissipation and low dispersion designed in Bogey & Bailly (2004), and makes use of explicit selective filtering as subgrid modelling. The computational domain extending up to 150 jet radii in the axial direction

is sufficiently large to contain a part of the self-similarity region of the jet. The main motivation is thus to provide reference solutions for the turbulence properties and energy budgets in the self-preserving jet, directly from the LES data without using any physical modelling for the turbulence statistics. Some quantities such as the second- and third-order moments of velocity fluctuations, the pressure–velocity correlations and the terms in the turbulent kinetic energy budget are calculated. As a validation, they are systematically compared with the experimental data given by Panchapakesan & Lumley (1993) for a jet at the same Reynolds number, when those data are available. The energy budget is also presented against the budget provided by Hussein *et al.* (1994). In this way, the assumptions made by Panchapakesan & Lumley and Hussein *et al.* for evaluating the energy terms across the jets will be discussed. Reliable information on jet turbulence physics are also expected by displaying, for instance, the role of pressure in the redistribution of energy between the velocity components. The relevance of some turbulence modellings will also be evaluated from the simulation results. For the characterization of the turbulent energy budget in the LES, an equation is derived from the compressible filtered Navier–Stokes equations and solved. The equation includes the dissipation due to the explicit filtering so that all the energy terms, whose sum will have to be nil, are directly computed. In Bogey & Bailly (2006c), which is a previous study dealing with the influence of the Reynolds number on energy dissipation in LES of round jets, the filtering dissipation was indeed obtained by difference. In the present work, it is then possible to assess the LES-RF method in a model flow by giving straightforward evidence of the filtering dissipation. The results obtained will allow us to investigate the filtering activity within the jet, and the way how it adjusts to the grid and to the flow features.

The present article is organized as follows. The LES equations and the equation for the turbulent kinetic energy, as well as the parameters of the simulation and of the jet flow, are provided in §2. The establishment of self-similarity along the jet axis is studied in §3, where the convergence of the turbulence statistics is also checked. Energy dissipation in the jet is then examined from the contributions of the filtering and of molecular viscosity. The features of turbulence and energy budgets across the jet self-similarity region are represented in §4. Concluding remarks are finally drawn, and the derivation of the energy budget equation including the filtering dissipation is reported in the Appendix.

2. Simulation parameters

2.1. LES methodology

LES is based on the filtered compressible Navier–Stokes equations, which can be written, following Vreman *et al.* (1997), in the following forms:

$$\frac{\partial \bar{p}}{\partial t} + \frac{\partial \bar{\rho} \tilde{u}_j}{\partial x_j} = 0, \quad (2.1)$$

$$\frac{\partial \bar{\rho} \tilde{u}_i}{\partial t} + \frac{\partial \bar{\rho} \tilde{u}_i \tilde{u}_j}{\partial x_j} = -\frac{\partial \bar{p}}{\partial x_i} + \frac{\partial \tilde{\tau}_{ij}}{\partial x_j} + \frac{\partial T_{ij}}{\partial x_j} + \mathcal{R}_i, \quad (2.2)$$

$$\frac{\partial \bar{\rho} \tilde{e}_t}{\partial t} + \frac{\partial ((\bar{\rho} \tilde{e}_t + \bar{p}) \tilde{u}_j)}{\partial x_j} = -\frac{\partial \tilde{q}_j}{\partial x_j} + \frac{\partial \tilde{\tau}_{ij} \tilde{u}_i}{\partial x_j} + \frac{\partial T_{ij} \tilde{u}_i}{\partial x_j} + \mathcal{R}_e, \quad (2.3)$$

where ρ represents the density, u_i the velocity, p the pressure, τ_{ij} the viscous stress tensor, e_t the total energy density and q_j the heat flux. The overbar denotes a filtered quantity, and the filtering is assumed to commute with time and spatial derivatives. The tilde denotes a quantity calculated from the filtered variables $\bar{\rho}$, $\bar{\rho}u_i$ and \bar{p} . Thus the calculated velocity is $\tilde{u}_i = \bar{\rho}u_i / \bar{\rho}$ using Favre filtering, and the calculated total energy is $\bar{\rho}\tilde{e}_t = \bar{p}/(\gamma - 1) + \bar{\rho}\tilde{u}_i\tilde{u}_i/2$ for a perfect gas, where γ is the specific heat ratio. The viscous stress tensor is defined by $\tilde{\tau}_{ij} = 2\tilde{\mu}(\tilde{s}_{ij} - \tilde{s}_{kk}\delta_{ij}/3)$, where $\tilde{s}_{ij} = (\partial\tilde{u}_i/\partial x_j + \partial\tilde{u}_j/\partial x_i)/2$. The viscosity $\tilde{\mu} = \mu(\tilde{T})$ is provided by Sutherland's law, and the temperature \tilde{T} is obtained using the state equation $\bar{p} = \bar{\rho}r\tilde{T}$. The heat flux is given by $\tilde{q}_j = -\lambda\partial\tilde{T}/\partial x_j$, where $\lambda = \tilde{\mu}c_p/\sigma$ is the thermal conductivity, σ is the Prandtl number and c_p is the specific heat at constant pressure. The low-pass filtering of the Navier–Stokes equations makes the so-called SGS terms appear in the right-hand side of (2.2) and (2.3). The most important term is the SGS turbulent stress tensor $T_{ij} = \bar{\rho}\tilde{u}_i\tilde{u}_j - \bar{\rho}u_iu_j$, whereas the other terms are included in \mathcal{R}_i and \mathcal{R}_e . They are described in Vreman, Geurts & Kuerten (1995) and in Geurts (2004).

Various SGS models are presented in Lesieur & Métais (1996), Meneveau & Katz (2000) and Domaradzki & Adams (2002). They have been specially analysed by *a priori* tests of their correlations with the SGS stress tensor. Most of the models are based on the use of eddy viscosity to account for the effects of the energy-dissipating scales. However, eddy viscosity, having the same functional form as molecular viscosity as pointed out by Domaradzki & Yee (2000), might be inappropriate and lead to an excessive damping of the larger scales and to an artificial decrease of the effective Reynolds number of the flow as shown by Bogey & Bailly (2005*a,b*). LES involving high-order/selective filterings have therefore been developed and applied successfully to isotropic turbulence, channel flows, jets and flow around an airfoil by Rizzetta *et al.* (2003), Mathew *et al.* (2003), Schlatter, Stolz & Kleiser (2004), Bogey & Bailly (2006*c*) and Marsden, Bogey & Bailly (2008). The basic idea in this LES approach based on relaxation filtering (LES-RF) is to control energy dissipation by minimizing the amount of dissipation on the larger scales and to diffuse energy only when it is transferred to the smaller scales discretized.

In the present simulation, the LES-RF approach is followed by using no structural modelling for the SGS stress tensor, but a selective filtering as a functional modelling of the subgrid dissipation. The filtering is applied explicitly to the density, momentum and pressure variables, $\bar{\rho}$, $\bar{\rho}u_i$ and \bar{p} , sequentially in the three Cartesian directions in order to remove the wavenumbers located near the grid cutoff wavenumber without significantly affecting the low wavenumbers accurately resolved by the numerical methods. In addition, for turbulent flows that are statistically stationary, the filtering process can deal with the fluctuating quantities only, which implies that it has no effect in a steady laminar flow.

The filtering of the density variable $\bar{\rho}$ in the x_1 direction yields, for instance, the following filtered quantity at grid point $(x_1(i_1), x_2(i_2), x_3(i_3))$,

$$\bar{\rho}_{i_1, i_2, i_3}^{sf} = \bar{\rho}_{i_1, i_2, i_3} - \sigma_d \sum_{j=-n}^n d_j (\bar{\rho}_{i_1+j, i_2, i_3} - \langle \bar{\rho}_{i_1+j, i_2, i_3} \rangle), \quad (2.4)$$

where σ_d is the filtering strength between 0 and 1, $\langle \cdot \rangle$ represents statistical averaging and d_j is the coefficient of a centred $(2n + 1)$ point filter. The mean quantities $\langle \cdot \rangle$ are computed by time averaging, using a moving window during the flow transient period.

2.2. Equation for the turbulent kinetic energy

An equation for the budget of the turbulent kinetic energy in compressible LES based on explicit filtering is derived. In order to include the terms associated with the filtering in the budget equation, one may notice that the filtering process (2.4) of the density variable is equivalent to the second-order explicit integration over the simulation time step Δt of the operator

$$D_{sf}^1(\bar{\rho})_{i_1, i_2, i_3} = -\frac{\sigma_d}{\Delta t} \sum_{j=-n}^n d_j (\bar{\rho}_{i_1+j, i_2, i_3} - \langle \bar{\rho}_{i_1+j, i_2, i_3} \rangle), \quad (2.5)$$

in the mass conservation equation, and that a similar remark can be made for the filtering of the momentum variables. This operator is similar to an operator of viscosity with high-order/optimized properties and to the relaxation term introduced by Stolz *et al.* (2001) in the LES equations.

The application of the explicit filtering to the density and the momentum variables can therefore be integrated into the right-hand side of (2.1) and (2.2) in the following way in the present study,

$$\frac{\partial \bar{\rho}}{\partial t} + \frac{\partial \bar{\rho} \tilde{u}_j}{\partial x_j} = D_{sf}(\bar{\rho}), \quad (2.6)$$

$$\frac{\partial \bar{\rho} \tilde{u}_i}{\partial t} + \frac{\partial \bar{\rho} \tilde{u}_i \tilde{u}_j}{\partial x_j} = -\frac{\partial \bar{p}}{\partial x_i} + \frac{\partial \tilde{\tau}_{ij}}{\partial x_j} + D_{sf}(\bar{\rho} u_i), \quad (2.7)$$

and the filtering operator D_{sf} is defined as

$$D_{sf}(\cdot) = D_{sf}^1(\cdot) + D_{sf}^2(\cdot) + D_{sf}^3(\cdot). \quad (2.8)$$

The developments required to derive the equations for the budgets of the turbulent kinetic energy are detailed in the Appendix. The budget equations obtained from (2.6) and (2.7) for the energy components are then given by

$$\begin{aligned} 0 = & \underbrace{-\frac{\partial}{\partial x_j} \left(\frac{1}{2} \langle \bar{\rho} u_i'^2 \rangle [u_j] \right)}_{\text{Mean flow convection}} \underbrace{-\langle \bar{\rho} u_i' u_j' \rangle \frac{\partial [u_i]}{\partial x_j}}_{\text{Production}} \underbrace{-\frac{1}{2} \frac{\partial}{\partial x_j} \langle \bar{\rho} u_i'^2 u_j' \rangle}_{\text{Turbulence diffusion}} \\ & \underbrace{-\frac{\partial}{\partial x_i} \langle p' u_i' \rangle}_{\text{Pressure diffusion}} \underbrace{+ \left\langle p' \frac{\partial u_i'}{\partial x_i} \right\rangle}_{\text{Pressure-dilatation term}} \underbrace{- \langle u_i' \rangle \frac{\partial \langle \bar{p} \rangle}{\partial x_i} - \left\langle \tilde{\tau}_{ij} \frac{\partial u_i'}{\partial x_j} \right\rangle}_{\text{Viscous dissipation}} \\ & + \underbrace{\frac{\partial}{\partial x_j} \langle u_i' \tilde{\tau}_{ij} \rangle + \langle u_i' D_{sf}(\bar{\rho} u_i) \rangle - \langle u_i' \tilde{u}_i D_{sf}(\bar{\rho}) \rangle + \frac{1}{2} \langle u_i'^2 D_{sf}(\bar{\rho}) \rangle}_{\text{Filtering dissipation}}, \quad (2.9) \end{aligned}$$

where statistical averaging is denoted by $\langle \cdot \rangle$ and Favre averaging by $[\cdot]$, yielding $[u_i] = \langle \bar{\rho} u_i \rangle / \langle \bar{\rho} \rangle$ for instance. The fluctuating velocity is defined by $u_i' = \tilde{u}_i - [u_i]$, and the turbulent kinetic energy by $\langle \bar{\rho} \rangle k = \langle \bar{\rho} u_i'^2 / 2 \rangle$. The second- and third-order moments of velocity are also evaluated using Favre averaging as

$$[u_i' u_j'] = \langle \bar{\rho} u_i' u_j' \rangle / \langle \bar{\rho} \rangle \quad \text{and} \quad [u_i'^2 u_j'] = \langle \bar{\rho} u_i'^2 u_j' \rangle / \langle \bar{\rho} \rangle.$$

The main terms in the energy equation are underlined and correspond to mean flow convection, production, turbulence diffusion, pressure diffusion, the pressure-dilatation

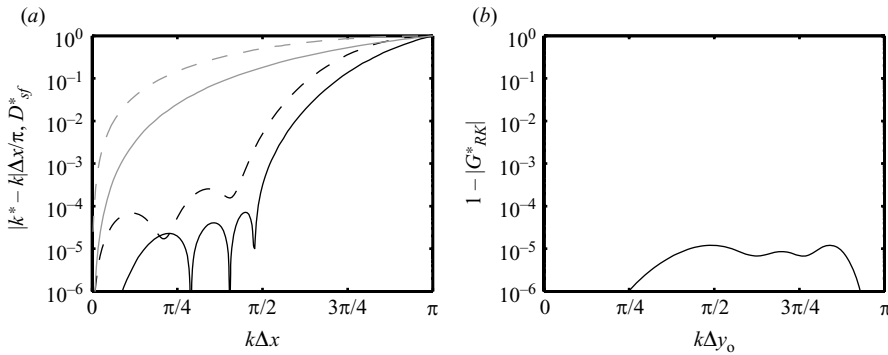


FIGURE 1. Representation using logarithmic scales: (a) phase error $|k^* - k|\Delta x/\pi$ introduced by (—) the present 11-point finite differences and (---) the second-order central finite differences, and damping rate D_{sf}^* of (— · —) the present 11-point selective filter and (— — —) the second-order central filter for a wavenumber k on a uniform Δx grid; (b) damping rate $1 - |G_{RK}^*|$ due to time integration, per iteration, for a wavenumber k convected at the jet exit velocity u_j on the Δy_0 grid in the present LES.

term, viscous dissipation and filtering dissipation, which can be calculated directly during the simulation.

In the same way, the equation for the budget of the Reynolds stress $[u'_1 u'_2]$ in the present LES writes as

$$\begin{aligned}
 0 = & -\frac{\partial}{\partial x_j} \langle \bar{\rho} u'_1 u'_2 \rangle [u_j] - \langle \bar{\rho} u'_2 u'_j \rangle \frac{\partial [u_1]}{\partial x_j} - \langle \bar{\rho} u'_1 u'_j \rangle \frac{\partial [u_2]}{\partial x_j} \\
 & - \frac{\partial}{\partial x_j} \langle \bar{\rho} u'_1 u'_2 u'_j \rangle - \frac{\partial}{\partial x_1} \langle p' u'_2 \rangle - \frac{\partial}{\partial x_2} \langle p' u'_1 \rangle + \left\langle p' \frac{\partial u'_2}{\partial x_1} \right\rangle \\
 & + \left\langle p' \frac{\partial u'_1}{\partial x_2} \right\rangle - \langle u'_2 \rangle \frac{\partial \langle p \rangle}{\partial x_1} - \langle u'_1 \rangle \frac{\partial \langle p \rangle}{\partial x_2} - \left\langle \tilde{\tau}_{1j} \frac{\partial u'_2}{\partial x_j} \right\rangle - \left\langle \tilde{\tau}_{2j} \frac{\partial u'_1}{\partial x_j} \right\rangle \\
 & + \frac{\partial}{\partial x_j} \langle u'_2 \tilde{\tau}_{1j} \rangle + \frac{\partial}{\partial x_j} \langle u'_1 \tilde{\tau}_{2j} \rangle + \langle u'_2 D_{sf} (\bar{\rho} u_1) \rangle + \langle u'_1 D_{sf} (\bar{\rho} u_2) \rangle \\
 & - \langle u'_2 \tilde{u}_1 D_{sf} (\bar{\rho}) \rangle - \langle u'_1 \tilde{u}_2 D_{sf} (\bar{\rho}) \rangle + \langle u'_1 u'_2 D_{sf} (\bar{\rho}) \rangle. \quad (2.10)
 \end{aligned}$$

2.3. Numerical algorithm

The LES is performed using schemes designed in Bogey & Bailly (2004), displaying low dissipation and low dispersion so that the scales discretized at least by four points are neither significantly distorted nor dissipated by the numerical algorithm. Fourth-order 11-point centred finite differences are used for space discretization, and a second-order 11-point selective filtering is applied explicitly to the flow variables as described previously, in order to remove grid-to-grid oscillations and to take into account the effects of the subgrid energy-dissipating scales. Time integration is carried out using a low-storage 6-stage Runge–Kutta algorithm. Moreover, due to the form of (2.1), (2.2) and (2.3), no second-derivation scheme is used.

The properties in the Fourier space of the finite differences and of the filter are illustrated in figure 1(a), where the phase error $|k^* - k|\Delta x/\pi$ of the derivation scheme and the damping rate D_{sf}^* of the filter are presented as functions of the wavenumber k for a uniform grid Δx . For the comparison, the phase error and the damping rate

obtained respectively for the second-order central finite differences and filter are also displayed. The phase error is based on the wavenumber k^* estimated by the finite differences, as defined in Tam & Webb (1993). The damping function D_{sf}^* of the filter is

$$D_{sf}^*(k\Delta x) = d_0 + \sum_{j=1}^5 2d_j \cos(jk\Delta x), \quad (2.11)$$

where d_j is the coefficient of the filtering process described by (2.4). The limits of accuracy of the derivation and the filtering schemes are both around $k\Delta x = \pi/2$. The larger scales which are accurately discretized by the finite differences are therefore expected to be affected in a negligible manner by the filtering, whereas the smaller scales which are badly calculated are damped.

The low dissipation of the Runge–Kutta scheme in the present jet simulation is now emphasized. Consider a perturbation characterized by the wavenumber k , convected at the velocity u_j in the grid region with the smaller mesh spacing, that is $\Delta y_0 = D/16$, near the jet axis. The amplification rate per time step Δt of this wave is given by the amplification factor $|G_{RK}^*|$ of the Runge–Kutta scheme for the angular frequency $\omega\Delta t = k^*u_j\Delta t$, where k^* is the wavenumber evaluated by the finite differences for the wavenumber k . The damping rate $1 - |G_{RK}^*|$ then obtained is plotted in figure 1(b). It is negligible for the whole range of wavenumbers $0 \leq k\Delta y_0 \leq \pi$, with a maximum value that is only around 10^{-5} . The dissipation due to the discretization schemes is thus very small, which can be essential for the computation of energy budgets.

2.4. Jet specifications

The isothermal round jet computed by LES in order to investigate its self-similarity region is characterized initially by a radius $r_0 = D/2$ and a velocity u_j , which provide a Mach number $M = 0.9$ and a Reynolds number $Re_D = 1.1 \times 10^4$. This Reynolds number corresponds to that of the jet studied experimentally by Panchapakesan & Lumley (1993), whereas the Reynolds number of the jet of Hussein *et al.* (1994) is 10^5 . Regarding the jet Mach number, it is significantly higher than in the two latter experiments, where inlet velocities of 27 m s^{-1} and 51 m s^{-1} were respectively specified. The difference in Mach number is however expected to have a negligible influence on the results obtained in the self-similar jets. In the self-similar region of the simulated jet, the centreline mean velocity will be about $u_j/10$ due to the velocity decay in the axial direction, implying that no appreciable compressible effect occurs.

The jet inflow conditions are modelled by imposing mean flow profiles while the random excitation described in Bogey, Bailly & Juvé (2003) is used to seed the turbulence. In practice, the mean axial velocity $u_0(r)$ at the jet inflow boundary is given by the following hyperbolic tangent profile:

$$\frac{u_0(r)}{u_j} = \frac{1}{2} + \frac{1}{2} \tanh\left(\frac{r_0 - r}{2\delta_\theta}\right),$$

where $r = \sqrt{y^2 + z^2}$, and $\delta_\theta = r_0/16$ is the initial momentum thickness of the annular shear layer. Pressure is taken as the ambient pressure, radial and azimuthal velocities are set to zero. The mean density profile $\rho_0(r)$ at the inflow is defined by the Crocco–Busemann relation

$$\frac{\rho_0(r)}{\rho_j} = \left(1 + \frac{\gamma - 1}{2} M^2 \frac{u_0(r)}{u_j} \left(1 - \frac{u_0(r)}{u_j}\right)\right)^{-1},$$

for an isothermal jet, where ρ_j is the inflow centreline density. In order to trigger the turbulence development, disturbances random in both time and space are added to the mean velocity profiles in the shear region for $x \simeq r_0$ throughout the simulation. The forcing has been developed to directly compute the noise generated by jets. Therefore the forcing disturbances are solenoidal velocity fluctuations involving various azimuthal modes with amplitude $\alpha = 0.01$, so that no significant spurious sound waves are generated. The azimuthal modes considered are modes from $n = 4$ to $n = 15$, as recommended by Bogey & Bailly (2005*b*) in a study of the influence of initial conditions on jet flow and noise.

At the boundaries except at the jet inflow, non-reflective conditions are applied. They consist of the far-field formulation of acoustic waves and rely on equations written for the fluctuating quantities. Small adjustment terms are consequently introduced near the limits of the domain with the aim of imposing mean ambient density and pressure. Note that the mean velocity is not specified outside the jet in order to allow the incoming of fluid into the computational domain and to ensure the entrainment of the fluid surrounding the jet into the flow. The detailed implementation can be found in Bogey & Bailly (2006*d*). A sponge zone combining grid stretching and Laplacian filtering is used at the jet outflow to dissipate turbulence before it reaches the boundary. The Laplacian filtering is applied to the flow fluctuations at a strength growing exponentially in the axial direction as in Bogey & Bailly (2002). In the same way as for pressure and density at the radiation boundaries, the mean flow variables in the sponge zone are also adjusted to match values following classical laws observed in self-similar jets, such as those given by (3.1) for the centreline velocity and the jet half-width.

2.5. Simulation parameters

The jet self-similarity region being reached 50 diameters downstream of the nozzle in the experiment by Panchapakesan & Lumley (1993), the present LES is performed using a Cartesian grid extending up to 150 radii in the axial direction x . A Cartesian coordinate system $(x_1, x_2, x_3) = (x, y, z)$, in which the velocity components are denoted equally as (u_1, u_2, u_3) and as (u, v, w) , is indeed chosen for its accuracy and its simplicity. It allows us in particular to avoid the axis singularity of a cylindrical system. The mesh grid contains $n_x \times n_y \times n_z = 651 \times 261 \times 261$ nodes, and the discretizations in the y and z directions are identical and symmetrical relative to the jet centreline. The mesh spacings in the x and y directions are illustrated in figure 2. In the axial direction, the grid spacing is initially $\Delta x = r_0/5$, and is then uniform with $\Delta x = r_0/4$ up to the mesh stretching used to form the sponge zone at the jet outflow. In the transverse direction, the grid spacing is also $\Delta y = r_0/4$ for $6.5r_0 \leq y \leq 23r_0$, but is smaller on the jet axis with $\Delta y = \Delta y_0 = r_0/8$. It increases for $y \geq 23r_0$ so that the sideline boundaries are located at $y = 33.5r_0$ from the jet axis.

Due to the explicit time integration, the time step is $\Delta t = 0.85 \Delta y_0 / c_0$. To ensure the convergence of high-order turbulence statistics, a very long simulation time was found to be necessary. The results reported in the article are obtained from 2.8×10^6 time steps, leading to a physical time $Tu_j/D = 1.2 \times 10^5$. The statistical averages of the turbulent quantities are more precisely evaluated by computing time averages after a transitory period of 10^5 time steps, when mean flow values are stationary. The statics are calculated using the Cartesian coordinates in the Oxy and Oxz sections, and then averaged and represented in the Oxy section. In what follows, (u, v, w) are therefore also used to denote the axial, radial and azimuthal velocities of the jet flow. Regarding the computational requirements, 22.4 Go of memory is

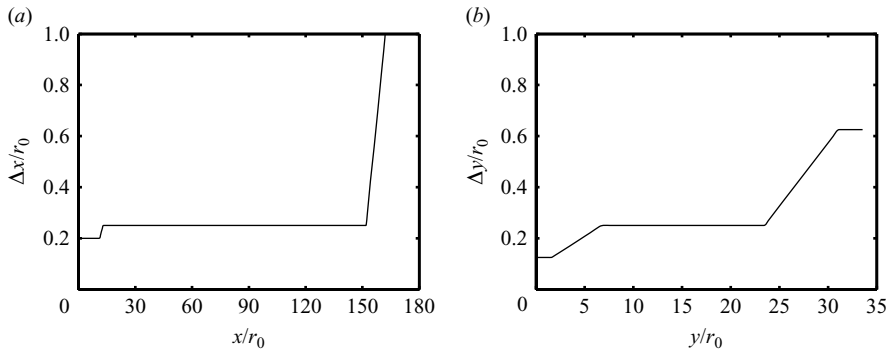


FIGURE 2. Mesh spacing: (a) in the axial direction, (b) in the transverse direction. The grid is symmetrically relative to the jet axis, and $y = z$.

necessary, and about 10 000 CPU hours have been consumed on SX5 and SX8 Nec computers.

Finally, the filtering is applied every second iteration to save computational time, with a strength $\sigma_d = 0.99$. The frequency of filtering and the value of σ_d are arbitrary, but from previous studies they are expected to have a weak influence on the results due to the selectivity of the filter. In Bogey & Bailly (2006b) indeed, applying the filtering every second or third time step provided very similar flow and dissipation features for transitional round turbulent jets. The dissipation rates obtained in the two cases in particular nearly collapse. In addition, the time step is small with respect to the characteristic time scales of the jet flow, especially in the self-similarity region. The frequency of application of the selective filtering, every second iteration, therefore appears appropriate for preventing an accumulation of energy at the smaller scales discretized.

3. Jet flow development and energy dissipation

3.1. Initial flow development

A snapshot of the vorticity field is presented in figure 3 in order to illustrate the development of the jet from the potential core region to a fully turbulent state. Vortical structures are initially generated in the shear layers, which merge at the end of the potential core. Farther downstream the radial spreading of the jet is visible, with turbulent structures found for instance at $y \simeq 20r_0$ from the centreline for $120r_0 \leq x \leq 150r_0$. The increase of the turbulent length scales as the jet develops, which follows a linear law according to Wygnanski & Fiedler (1969), is also noticed.

Some flow features obtained for $x \leq 50r_0$ are shown in figure 4. In the same way as the inflow parameters themselves, the early development of the jet can also be regarded as initial conditions of the self-similar jet. The results in figure 4 are presented with this aim in view. They are not compared with experimental data because no corresponding data are provided by Panchapakesan & Lumley (1993). The momentum thickness $\delta_\theta = r_0/16$ of the inflow shear layer in the present jet is also quite large with respect to the values observed in experiments, and the initial development of transitional jets depends strongly on the inflow parameters as it has been evidenced in Bogey & Bailly (2005b).

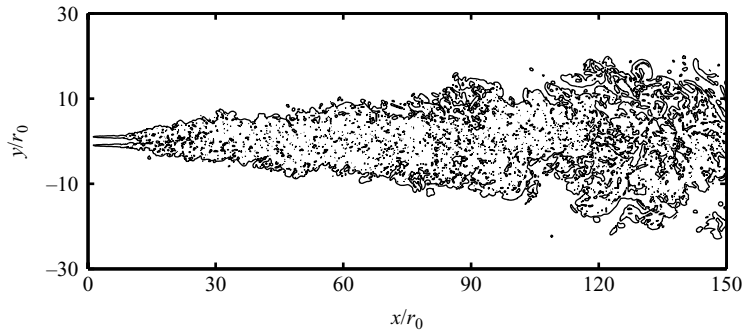


FIGURE 3. Snapshot of the vorticity field in the plane $z=0$. Representation of the two contours associated with the magnitudes of vorticity norm $|\omega| \times x/u_j = [4, 40]$.

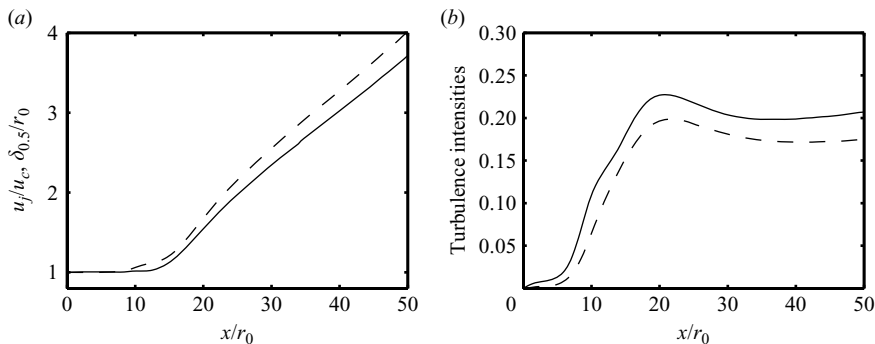


FIGURE 4. Axial variations for $x \leq 50r_0$: (a) —, inverse of centreline mean axial velocity u_j/u_c and ---, jet half-width $\delta_{0.5}/r_0$; (b) centreline turbulence intensities: —, $[u'u']^{1/2}/u_c$ and ---, $[v'v']^{1/2}/u_c$.

The variations of the inverse of the centreline mean velocity $u_c = [u](y=0)$, and of the jet half-width $\delta_{0.5}$, defined by $[u](y=\delta_{0.5})=u_c/2$, are plotted in figure 4(a). The end of the potential core, indicated here by $u_c(x_c)=0.95u_j$, is located at $x_c=13.5r_0$. The mean flow development, namely the velocity decay and the growth of the jet half-width, is seen to be rapid just downstream of the end of the potential core, and then occurs more slowly for $x \geq 25r_0$. The profiles of the axial and radial turbulence intensities along the jet centreline are presented in figure 4(b). Both components initially rise and reach a peak around $x=20r_0$. They finally increase again from $x \simeq 35r_0$ at a low rate, as they progressively tend towards the self-similarity values which will be exhibited later in figure 7.

3.2. Establishment of self-similarity

The establishment of self-similarity in the jet is investigated by considering the evolution of some flow features in the axial direction for $x \geq 50r_0$. The aim here is to determine whether the mean and the turbulent flows achieve similarity in the present finite computational domain, and whether the axial distances required are comparable with the experimental results of Panchapakesan & Lumley (1993). The convergence

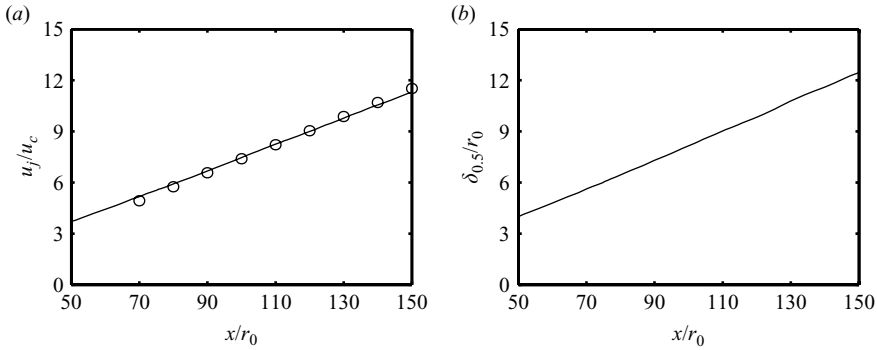


FIGURE 5. Axial variations over $50r_0 \leq x \leq 150r_0$: (a) inverse of centreline mean axial velocity u_j/u_c (o, Panchapakesan & Lumley (1993) data shifted by $10r_0$ in the axial direction for the comparison); (b) jet half-width $\delta_{0.5}/r_0$.

of the turbulence statistics, including the third-order velocity moments and the terms of the energy budget, is also examined.

The mean flow is characterized from the centreline mean velocity u_c and the jet half-width $\delta_{0.5}$, which are given, in a self-preserving jet, respectively by

$$\frac{u_c}{u_j} = B \times \frac{D}{(x - x_0)} \quad \text{and} \quad \delta_{0.5} = A \times (x - x_0), \quad (3.1)$$

where B and A , namely the decay constant and the spreading rate, are two constants, and x_0 denotes a virtual origin. The profiles calculated for u_j/u_c and $\delta_{0.5}/r_0$ are plotted in figure 5. Both appear to roughly increase linearly for $x \geq 50r_0$. In addition, the centreline velocity in figure 5(a) seems to agree fairly well with the corresponding data of Panchapakesan & Lumley (1993). For the comparison, the data of Panchapakesan & Lumley are however shifted by $10r_0$ in the axial direction, which is indicative of different lengths of potential core in the simulation and in the experiment. This discrepancy is certainly due to differences in the inflow conditions.

To investigate more quantitatively the mean flow self-similarity, the local decay constant B' and the local spreading rate A' are considered. They are evaluated from the profiles of figure 5 in the following way,

$$\frac{1}{B'} = \frac{d(u_j/u_c)}{d(x/D)} \quad \text{and} \quad A' = \frac{d\delta_{0.5}}{dx}, \quad (3.2)$$

and represented in figure 6. The two curves of $1/B'$ and A' , albeit not perfectly smooth because of the derivations in expressions (3.2), are found to display asymptotic values for about $x \geq 100r_0$. The mean flow therefore becomes self-similar at 100 radii from the inflow boundaries. The constants in the self-preserving region, obtained by averaging B' and A' over $100r_0 \leq x \leq 140r_0$, are $B = 6.4$ and $A = 0.087$. For comparison, Panchapakesan & Lumley (1993) measured constants $B = 6.06$ and $A = 0.096$ in their self-preserving jet. The present results are slightly different, which can be due to the fact that the details of self-similarity may depend on the jet initial conditions, as supported by the DNS results of Boersma *et al.* (1998). Further works would be required to clarify this point.

Our attention now turns to the self-similarity of the turbulent flow, which is usually observed in experiments when the turbulence intensities $[u'_i u'_i]^{1/2}/u_c$ are constant on the jet axis. The axial variations of the centreline values and of the

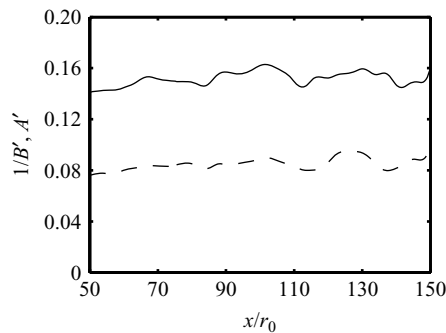


FIGURE 6. Axial variations over $50r_0 \leq x \leq 150r_0$: —, inverse of local decay constant $1/B'$; - - -, local spreading rate A' .

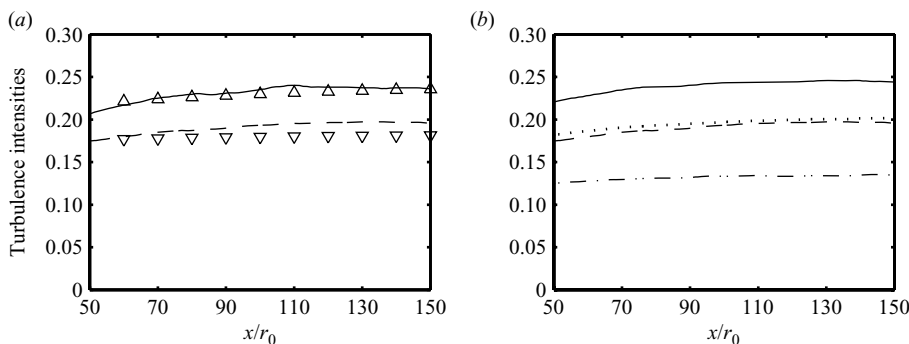


FIGURE 7. Axial variations over $50r_0 \leq x \leq 150r_0$ of turbulence intensities (a) along the jet centreline and (b) peak values across the jet: $[u'u']^{1/2}/u_c$ (—, LES; \triangle , Panchapakesan & Lumley (1993)), $[v'v']^{1/2}/u_c$ (- - -, LES; ∇ , Panchapakesan & Lumley), $[w'w']^{1/2}/u_c$ (....., LES) and $[-u'v']^{1/2}/u_c$ (- · - ·, LES).

peak values across the present jet of the turbulence intensities are presented in figure 7. As reported in Wygnanski & Fiedler (1969) and in Panchapakesan & Lumley (1993), the axial component may reach its self-similarity value slightly before the other components. Nevertheless, all the components display fairly constant values from $x = 120r_0$, which suggests that turbulence becomes self-similar around this axial location. This behaviour is in good agreement with the measurements of Panchapakesan & Lumley obtained for a jet at the same Reynolds number, as indicated by the centreline profiles of figure 7(a). Therefore, the use of the explicit filtering, unlike that of an eddy viscosity SGS model in Bogey & Bailly (2006*b,c*), does not appear to artificially accelerate the transition towards self-similarity, and decrease the Reynolds number of the flow. Self-similarity values $[u'u']^{1/2}/u_c = 0.24$ and $[v'v']^{1/2}/u_c = 0.20$ are noted on the jet axis, which compare well with the data of Panchapakesan & Lumley exhibiting $[u'u']^{1/2}/u_c = 0.24$ and $[v'v']^{1/2}/u_c = 0.19$.

The variations of the peak values across the jet of the third-order velocity moments $[u'_i u'_j u'_k]/u_c^3$, and of the dominant terms in the energy budget, are finally drawn in figures 8 and 9 to check the self-similarity and the convergence of the higher order statistics. The energy terms are computed explicitly from (2.9). They correspond to mean convection, production, dissipation, turbulence diffusion, pressure diffusion and dissipation, where dissipation is the sum of the viscous dissipation and of the

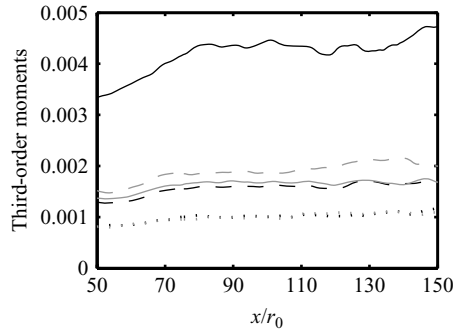


FIGURE 8. Axial variations over $50r_0 \leq x \leq 150r_0$ of peak values across the jet of third-order velocity moments: —, $[u'u'u']/u_c^3$; ---, $[v'v'u']/u_c^3$; ·····, $[w'w'u']/u_c^3$; — · —, $[u'u'v']/u_c^3$; - - - - -, $[v'v'v']/u_c^3$; ·····, $[w'w'v']/u_c^3$.

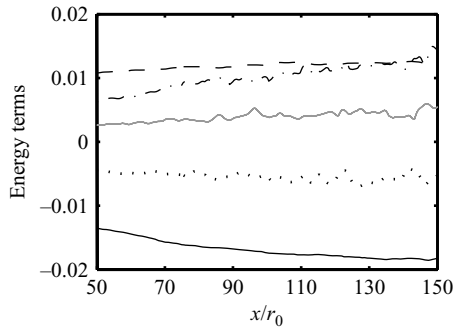


FIGURE 9. Axial variations over $50r_0 \leq x \leq 150r_0$ of peak values across the jet of terms in the turbulent kinetic energy budget: ·····, mean flow convection; — · —, production; ·····, turbulence diffusion; —, pressure diffusion; — · —, dissipation (curves normalized by $\rho_c u_c^3 \delta_{0.5}$, ρ_c : centreline mean density).

filtering dissipation. The profiles show short oscillations that are of low magnitude, which supports the assertion that the convergence in time of the different terms is satisfactory. The convergence is however much higher in figure 8 for the component $[v'v'v']/u_c^3$ than for the component $[u'u'u']/u_c^3$, and in figure 9 for production and dissipation than for turbulence and pressure diffusions. Furthermore, as the turbulence intensities in figure 7, the different terms in figures 8 and 9 appear to tend to constant values as the axial distance increases, asymptotic values being obtained around $x = 120r_0$.

Based on the present trends in the axial direction, self-similarity is found for $x \geq 100r_0$ for the mean flow, but farther downstream for the turbulent flow. The profiles across the self-preserving jet presented in what follows have therefore been obtained by averaging the LES results over $100r_0 \leq x \leq 140r_0$ for the mean flow, but over $125r_0 \leq x \leq 145r_0$ for the turbulent statistics.

To further quantify the deviation from self-similarity, the percentage difference between flow quantities over $50r_0 \leq x \leq 150r_0$ and their assumed self-similar values are calculated. The rates obtained for the centreline mean velocity and the jet half-width with respect to the self-similarity expressions (3.1) in which constants A , B and x_0 are evaluated over $100r_0 \leq x \leq 140r_0$ are presented in figure 10(a). For $x \geq 90r_0$, the percentage deviations are very small. The mean absolute deviations

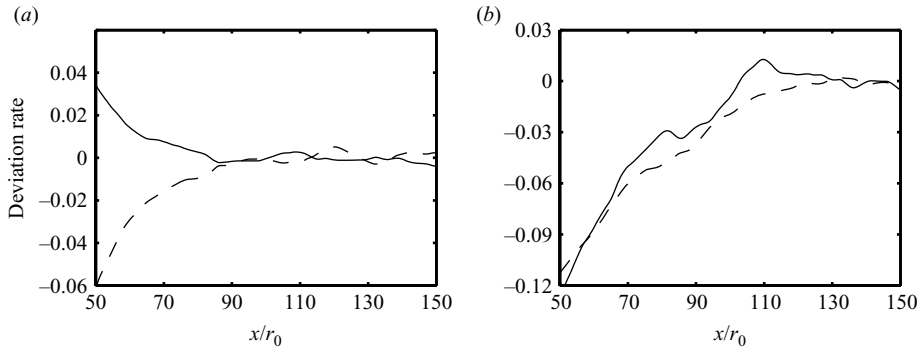


FIGURE 10. Percentage of deviation between flow quantities over $50r_0 \leq x \leq 150r_0$ and their self-similarity values: (a) —, centreline mean axial velocity u_c ; - - -, jet half-width $\delta_{0.5}$; (b) centreline turbulence intensities: —, $[u'u']^{1/2}/u_c$; - - -, $[v'v']^{1/2}/u_c$.

over $100r_0 \leq x \leq 140r_0$ are even more precisely 0.21 % for u_c and 0.11 % for $\delta_{0.5}$. The percentage differences between the centreline turbulence intensities and their asymptotic values averaged over $125r_0 \leq x \leq 145r_0$ are also shown in figure 10(b). As shown previously, the deviations decrease with the axial position and become small for $x \geq 120r_0$. In this case, the mean absolute deviations over $125r_0 \leq x \leq 145r_0$ are respectively 0.16 % and 0.14 % for the axial and the radial components.

3.3. Energy dissipation and filtering activity

This section focuses on the dissipation mechanisms involved in the LES, namely the viscous and the filtering dissipations, given respectively by

$$\langle \epsilon_\mu \rangle = - \left\langle \tilde{\tau}_{ij} \frac{\partial u'_i}{\partial x_j} \right\rangle \quad \text{and} \quad \langle \epsilon_{sf} \rangle = \langle u'_i D_{sf}^j (\overline{\rho u_i}) \rangle \quad (3.3)$$

in (2.9). In Bogey & Bailly (2006c), their contributions were evaluated in jets to examine the Reynolds number effects on energy dissipation. The filtering dissipation was however obtained by difference. In the present study, this dissipation is estimated explicitly from the LES fields, and to assess the importance of the filtering, we define, following Geurts & Fröhlich (2002), the subgrid activity parameter

$$s = \frac{\langle \epsilon_{sf} \rangle}{\langle \epsilon_{sf} \rangle + \langle \epsilon_\mu \rangle}, \quad (3.4)$$

which represents also the filtering activity parameter in the present work.

The profiles of the viscous and filtering dissipations along the jet axis are presented in figure 11(a). The sum of the different terms in (2.9) is plotted as well. It is nearly zero, which suggests that the computation of the energy budget is performed in a suitable manner, and that energy is not significantly damped by the low-dissipation Runge–Kutta algorithm. The magnitudes of viscous and filtering dissipations vary with the axial distance. As the jet develops in the downstream direction, the contribution of the filtering decreases, whereas that of viscosity increases, which leads to the lowering of the filtering activity parameter s in figure 11(b). Indeed, about two-thirds of the energy dissipation is provided by the filtering at $x = 50r_0$, but only one-third at $x = 150r_0$. This behaviour is due to the growth of the turbulent length scales along the jet axis. The mesh spacing being uniform between $x = 50r_0$ and $150r_0$, a more important part of the energy-dissipating scales is then calculated, which reduced the subgrid activity,

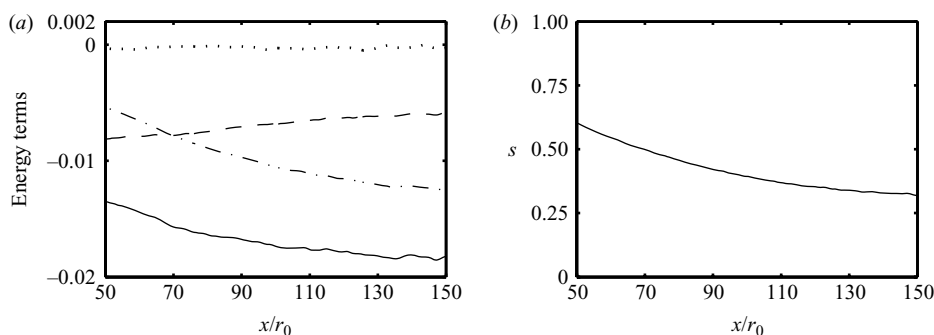


FIGURE 11. Variations along the jet centreline: (a) $-\cdot-\cdot-$, viscous dissipation; $---$, filtering dissipation; $---$, total dissipation; \cdots , sum of all the terms in the turbulent kinetic energy budget (curves normalized by $\rho_c u_c^3 \delta_{0.5}$); (b) filtering activity parameter s .

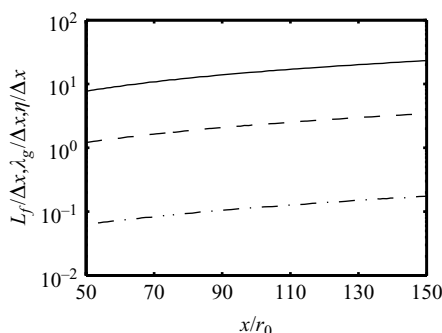


FIGURE 12. Variations along the jet centreline of the ratios between the axial integral length scale, the transverse Taylor and Kolmogorov scales and the axial mesh spacing: $---$, $L_f/\Delta x$; $---$, $\lambda_g/\Delta x$; $-\cdot-\cdot-$, $\eta/\Delta x$.

and hence the role played by the filtering. The contribution of the explicit filtering therefore appears to adjust by itself to the flow development as expected.

To illustrate quantitatively both the growth of the flow length scales in the downstream direction and the LES resolution, the ratios between typical turbulence length scales and the mesh spacing Δx along the jet axis are represented in figure 12. The axial integral length scale is evaluated from the law $L_f = 0.0385x$ observed experimentally in Wygnanski & Fiedler (1969) as well as numerically in Bogey & Bailly (2006d), while the transverse Taylor scale and the Kolmogorov scale are calculated using the relations of isotropic turbulence, which are $\lambda_g = (15L_f \nu / [u' u']^{1/2})^{1/2}$ and $\eta = (L_f^{1/4} (\nu / [u' u']^{1/2})^{3/4}$. As the jet develops, the length scales increase as expected, and consequently $L_f/\Delta x = 7.7$, $\lambda_g/\Delta x = 1.2$ and $\eta/\Delta x = 0.06$ at $x = 50r_0$, whereas $L_f/\Delta x = 21$, $\lambda_g/\Delta x = 3.1$ and $\eta/\Delta x = 0.16$ at $x = 135r_0$ in the self-similar jet. In this region, the integral length scale is well resolved, and the Taylor scale is discretized.

The dissipation rates obtained across the self-preserving jet for the turbulent kinetic energy are represented in figure 13. As previously in figure 11(a), the sum of the different energy terms is checked to be nearly zero. The viscous dissipation is higher than the filtering dissipation, whatever the radial position may be. The ratio between the two contributions however seems to vary with the radial position,

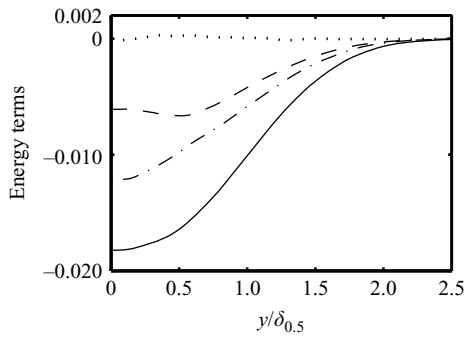


FIGURE 13. Profiles across the self-similar jet averaged over $125r_0 \leq x \leq 145r_0$: \cdots , viscous dissipation; $---$, filtering dissipation; $—$, total dissipation; $-\cdots-$, sum of all the terms in the budget for the turbulent kinetic energy k (curves normalized by $\rho_c u_c^3 \delta_{0.5}$).

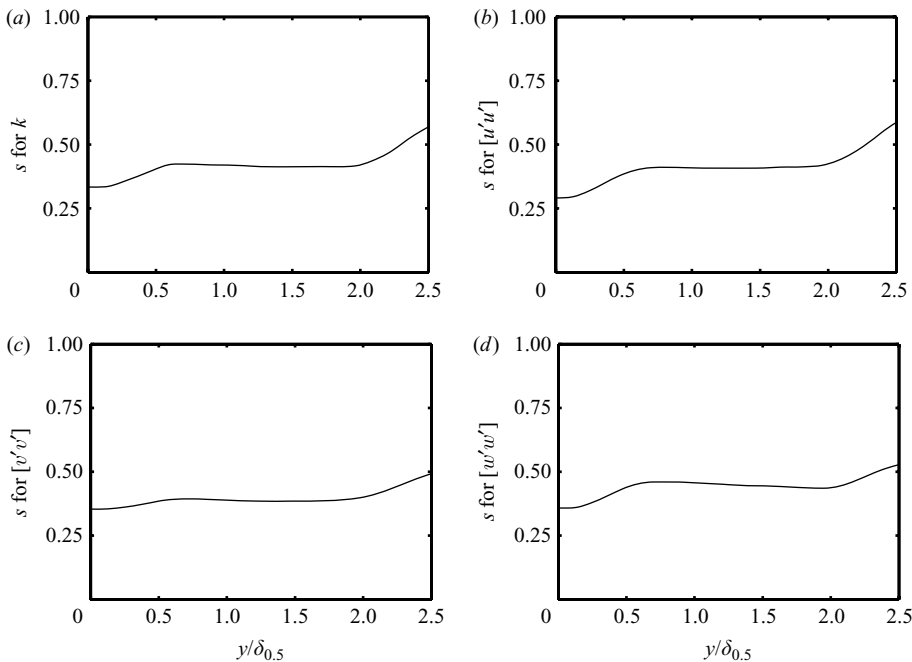


FIGURE 14. Profiles across the self-similar jet, averaged over $125r_0 \leq x \leq 145r_0$, of the filtering activity parameter s calculated for (a) k , (b) $[u'u']$, (c) $[v'v']$ and (d) $[w'w']$.

the filtering contribution appearing, for instance, to decrease in the vicinity of the centreline.

To quantify the variations of the dissipation rates across the jet, the filtering activity parameter s is computed for the turbulent kinetic energy and for the energy components, and is presented in figure 14. The shapes of the curves obtained are very similar, with a minimum value close to the centreline, a slight increase before a zone displaying nearly constant values for $0.6 \leq y/\delta_{0.5} \leq 2$ and a final growth for $y/\delta_{0.5} \geq 2$. The filtering activity is therefore connected with the radial grid spacing shown previously in figure 2(b). It is lower on the jet axis where the radial grid spacing is smaller with $\Delta y = r_0/8$, it does not vary significantly in the central zone

	k	$[u'u']$	$[v'v']$	$[w'w']$
$s(y=0)$	0.334	0.291	0.354	0.358
$s(y/\delta_{0.5}=1.25)$	0.414	0.407	0.385	0.449

TABLE 1. Filtering activity parameter s calculated for the turbulent kinetic energy and for the three energy components, averaged over $125r_0 \leq x \leq 145r_0$, at $y=0$ and at $y/\delta_{0.5}=1.25$.

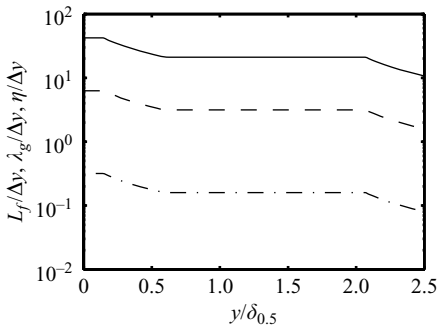


FIGURE 15. Profiles across the self-similar jet at $x=135r_0$ of the ratios: —, $L_f/\Delta y$; - - -, $\lambda_g/\Delta y$; - · - ·, $\eta/\Delta y$.

where the grid spacing is uniform with $\Delta y=r_0/4$ and it increases in the vicinity of the sideline boundary where the grid is stretched. The influence of the mesh grid is also illustrated in table 1 reporting the values of the parameter s at $y=0$ and at $y/\delta_{0.5}=1.25$. Values of 0.335 and 0.415 are for instance respectively found from the turbulent kinetic energy.

Table 1 allows us also to compare the filtering activity for the different energy components. On the jet axis, where $\Delta y=\Delta z$, the filtering activities are the same for the components $[v'v']$ and $[w'w']$ due to the rotation invariance of the flow in a cross-section. The filtering activity for the component $[u'u']$ displays another value because of the anisotropy of the flow and of the mesh ($\Delta x=2\Delta y$) in the x - y section. At the radial position $y/\delta_{0.5}=1.25$, both the grid and the flow are anisotropic ($\Delta y=\Delta x=\Delta z/2$ in particular). As a result, the filtering activity differs according to the energy components, ranging from 0.385 for the component $[v'v']$ to 0.449 for the component $[w'w']$. The contribution of the explicit filtering to energy dissipation is thus shown to depend on both the grid spacing and the flow features.

The ratios between turbulence length scales and the radial grid spacing across the self-similar jet at $x=135r_0$ are moreover displayed in figure 15. The length scales being assumed to vary in a negligible manner across a given section, their values are those calculated on the centreline. The ratios in figure 15 thus decrease with the radial position as Δy increases. However, whatever the radial position may be, the integral length scale is well resolved, and the Taylor scale is discretized, with for instance $\lambda_g/\Delta y=3.1$ at the position $y/\delta_{0.5}=1.25$.

4. Turbulence across the self-similarity flow region

4.1. Mean velocity

The profiles across the jet of the mean axial and radial velocities normalized with u_c , obtained over the range $100r_0 \leq x \leq 140r_0$, are represented in figure 16. The LES

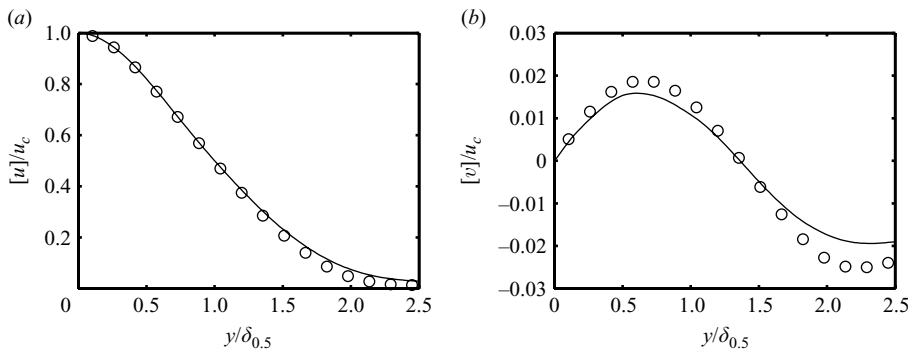


FIGURE 16. Profiles across the self-similar jet. (a) mean axial velocity $[u]/u_c$ and (b) mean radial velocity $[v]/u_c$: —, LES; o, Panchapakesan & Lumley (1993). The LES profiles are averaged over $100r_0 \leq x \leq 140r_0$.

mean axial velocity agrees very well with the self-similarity profile measured by Panchapakesan & Lumley (1993). A good similarity is also seen for the mean radial velocity profile predicted by the LES and the profile calculated by Panchapakesan & Lumley from the mean axial velocity using the continuity equation. The negative values of the mean radial velocity for large distances from the centreline indicate that the fluid surrounding the jet fluid is entrained into the flow. The boundary conditions in the simulation therefore appear appropriate for allowing the incoming of fluid into the computational domain.

4.2. Second-order velocity moments

The radial profiles of the turbulence intensities, computed by averaging over $125r_0 \leq x \leq 145r_0$, are shown in figure 17. Their shapes and their magnitudes compare well with the experimental results of Panchapakesan & Lumley (1993) measured using a shuttle-mounted x -wire hot-wire probe in a self-preserving jet at the same Reynolds number as the simulated jet. The agreement is particularly good for the axial component $[u'u']$ and for the Reynolds stress $[-u'v']$. The radial and azimuthal components $[v'v']$ and $[w'w']$ are slightly higher than the measurements, but their difference in shape is remarkably reproduced. The profiles of turbulence intensities measured by Wygnanski & Fiedler (1969) using SHW (stationary hot-wire) and by Hussein *et al.* (1994) using both SHW and LDA (laser-Doppler anemometry) are not plotted here, because they have been obtained for jets at Reynolds number $Re_D = 10^5$. They have been however found to display higher values with peaks around $[u'u']^{1/2}/u_c = 0.28$ and $[v'v']^{1/2}/u_c = 0.23$ for instance, which could be attributed at least partially to Reynolds number effects, as suggested by recent results obtained by Deo, Mi & Nathan (2008) for plane jets.

4.3. Third-order velocity moments

The third-order moments of velocity fluctuations $[u'_i u'_j u'_k]/u_c^3$ calculated in the self-preserving jet are presented in figure 18. These terms are important because their gradients determine the turbulence diffusion of turbulent kinetic energy in (2.9). The axial fluxes of the energy components, which are $[u'u'u']$, $[v'v'u']$ and $[w'w'u']$, are shown in figures 18(a) and 18(d), and the radial fluxes $[u'u'v']$, $[v'v'v']$ and $[w'w'v']$ in figures 18(b) and 18(c).

Compared with Panchapakesan & Lumley (1993) measurements, the agreement is generally good, as illustrated for example by results in figure 18(d). The profile for

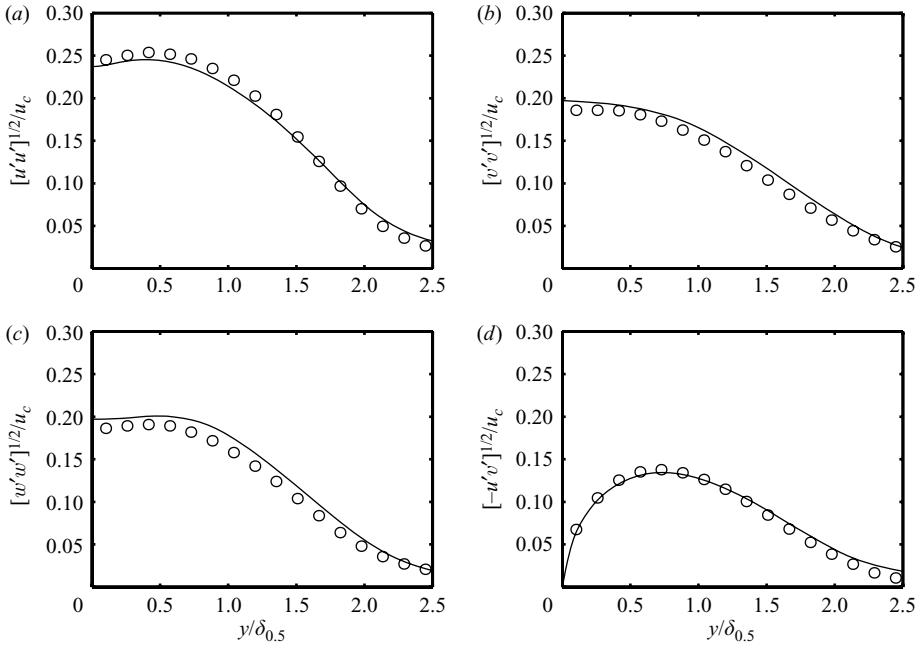


FIGURE 17. Profiles of turbulence intensities across the self-similar jet; (a) $[u'u']^{1/2}/u_c$, (b) $[v'v']^{1/2}/u_c$, (c) $[w'w']^{1/2}/u_c$ and (d) $[-u'v']^{1/2}/u_c$: —, LES; \circ , Panchapakesan & Lumley (1993). The LES profiles are averaged over $125r_0 \leq x \leq 145r_0$.

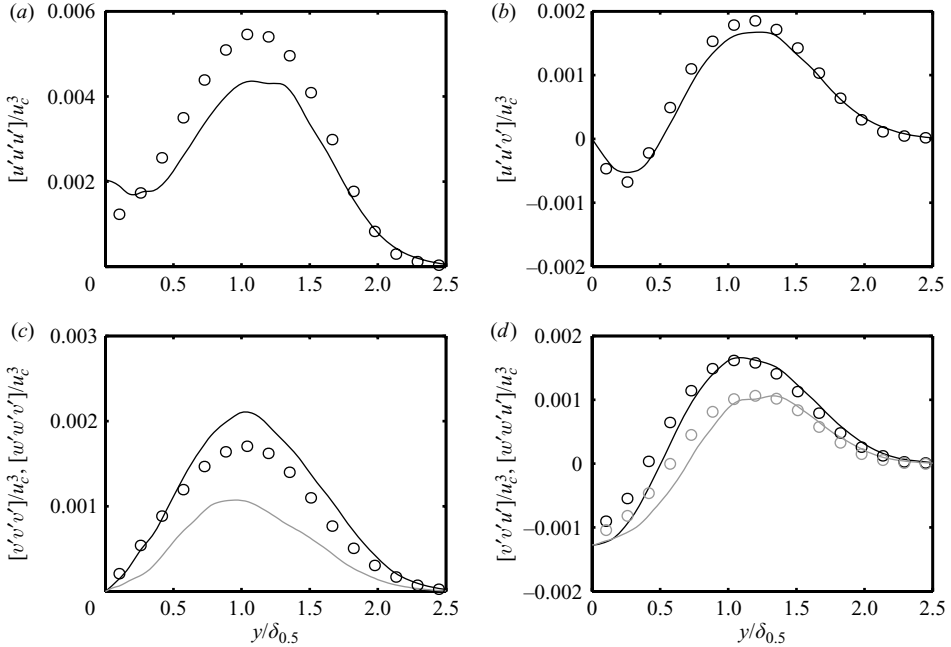


FIGURE 18. Profiles of third-order velocity moments across the self-similar jet: (a) $[u'u'u']/u_c^3$ and (b) $[u'u'v']/u_c^3$ (—, LES; \circ , Panchapakesan & Lumley (1993)), (c) $[v'v'v']/u_c^3$ (—, LES; \circ , Panchapakesan & Lumley) and $[w'w'v']/u_c^3$ (—, LES), (d) $[v'v'u']/u_c^3$ (—, LES; \circ , Panchapakesan & Lumley) and $[w'w'u']/u_c^3$ (—, LES; \circ , Panchapakesan & Lumley). The LES profiles are averaged over $125r_0 \leq x \leq 145r_0$.

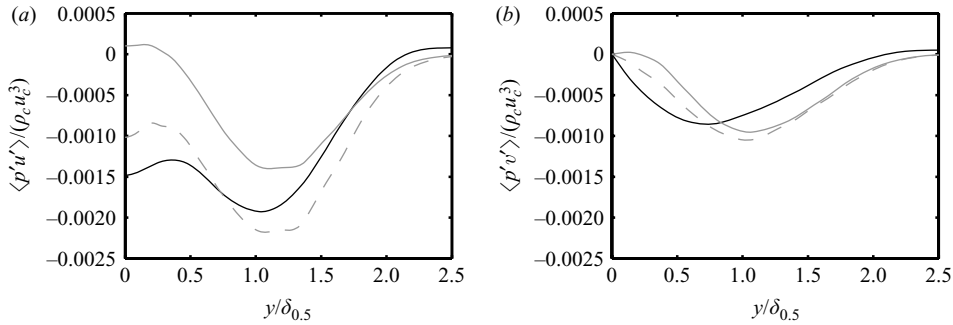


FIGURE 19. Profiles across the self-similar jet, averaged over $125r_0 \leq x \leq 145r_0$ of: —, pressure–velocity correlations: (a) $\langle p'u' \rangle / (\rho_c u_c^3)$ and (b) $\langle p'v' \rangle / (\rho_c u_c^3)$, ——— modellings suggested by Lumley (1978): (a) $-[u'_i u'_i u'] / (5u_c^3)$ and (b) $-[u'_i u'_i v'] / (5u_c^3)$, and - - - terms: (a) $-[u'u'u'] / (2u_c^3)$ and (b) $-[v'v'v'] / (2u_c^3)$.

$[u'u'u']$ in figure 18(a) also exhibits a shape similar to the Panchapakesan & Lumley curve, but with a lower magnitude. At this stage it is difficult to state about the origin of the discrepancy, but it can be mentioned that the corresponding profiles obtained by Wygnanski & Fiedler (1969) and Hussein *et al.* (1994) using SHW display peaks around 4×10^{-3} as the LES profile. For the third-order velocity moments, the data are indeed scattered according to the experimental techniques, as pointed out by Hussein *et al.* and Panchapakesan & Lumley. Hussein *et al.* obtained for instance significant differences in shape, slope and amplitude between the SHW and LDA measurements, with the SHW failing in particular to detect negative values of $[u'u'v']$ near the centreline. The LES results in figure 18 therefore tend to support the accuracy of the data of Panchapakesan & Lumley for the jet considered at Reynolds number $Re_D = 1.1 \times 10^4$.

Furthermore, the curve for $[w'w'v']$ in figure 18(c) has a magnitude which is about half that obtained for $[v'v'v']$. With this result in mind, it is useful recalling that the approximation $[w'w'v'] = [v'v'v']$ is frequently made in experimental works, including Panchapakesan & Lumley (1993) and Hussein *et al.* (1994), to evaluate the turbulence diffusion term in the energy budget because of the difficulty to measure the former quantity. The numerical results indicate that this approximation is very crude, which might generate inaccuracies in experimental energy budgets. This point will be discussed later in §4.5.

4.4. Pressure–velocity correlations

The pressure–velocity correlations $\langle p'u' \rangle$ and $\langle p'v' \rangle$ normalized by $\rho_c u_c^3$, obtained across the self-similarity jet flow, are shown in figure 19. The LES solutions are of interest because the gradients of pressure–velocity correlations govern pressure diffusion in (2.9) for the turbulent energy budget. As in the previous section for the velocity moment $[w'w'v']$, they can also be considered as reference solutions because the measurements of such quantities are complicated, which usually leads to indirect approximations. Sami (1967) for instance evaluated the correlations $\langle p'u' \rangle$ in jets by the subtraction of terms involving second-order moments of pressure and axial velocity, whereas Hussein *et al.* (1994) estimated $\langle p'v' \rangle$ from energy dissipation curves assuming isotropic or axisymmetric turbulence.

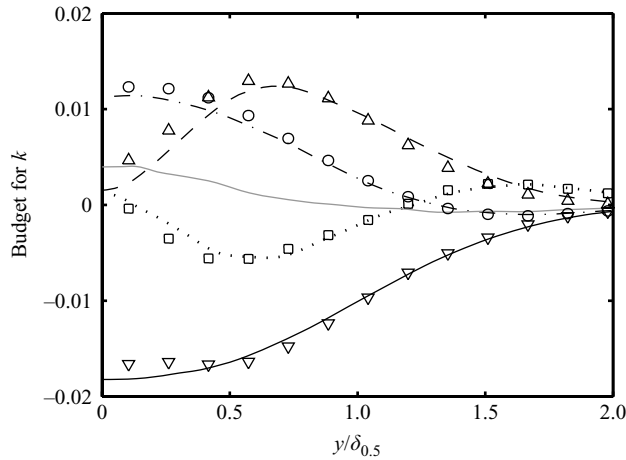


FIGURE 20. Budget for the turbulent kinetic energy k across the self-similar jet, compared with data of Panchapakesan & Lumley (1993): mean flow convection (---, LES; \circ , Panchapakesan & Lumley), production (---, LES; \triangle , Panchapakesan & Lumley), dissipation (—, LES; ∇ , Panchapakesan & Lumley), turbulence diffusion (·····, LES; \square , Panchapakesan & Lumley) and pressure diffusion (—, LES). The curves are normalized by $\rho_c u_c^3 \delta_{0.5}$, and averaged over $125r_0 \leq x \leq 145r_0$ for the LES.

As reported by Pope (2000), Lumley (1978) proposed to model the pressure–velocity correlations using third-order velocity moments as

$$\langle p'u'_i \rangle = -\frac{1}{5}\rho \langle u'_j u'_j u'_i \rangle. \quad (4.1)$$

Following this suggestion, the quantities $-[u'_j u'_j u'_i]/5$ and $-[u'_j u'_j v']/5$, normalized by u_c^3 , are represented in figure 19. Similarities are observed respectively with the correlations $\langle p'u' \rangle$ and $\langle p'v' \rangle$, but appreciable discrepancies are seen both in shape and in magnitude, especially near the centreline. Other modellings of pressure–velocity correlations based on third-order velocity moments have therefore been arbitrarily tested. Fairly good comparisons are obtained in figure 19(a) between the correlation $\langle p'u' \rangle$ and the term $-[u'u'u']/2$, and in figure 19(b) between $\langle p'v' \rangle$ and $-[v'v'v']/2$.

4.5. Turbulent kinetic energy budget

The budget for the turbulent kinetic energy in the jet self-similarity region is presented in figures 20 and 21. All the terms in (2.9) are calculated explicitly from the LES data, and their sum is checked to be nearly zero in figure 13. Reference solutions are obtained because no *a priori* assumption on the turbulence field is made, which allows us to complement the experimental data and to discuss the turbulence modellings used in Panchapakesan & Lumley (1993) and Hussein *et al.* (1994). The main energy terms correspond to mean flow convection, production, dissipation, turbulence diffusion and pressure diffusion. The pressure–strain correlation term is negligible because of the incompressibility of the flow in the self-preserving region, where, according to the velocity decay of figure 5(a), the centreline mean axial velocity is for instance only $[u]/c_0 \simeq 0.1$ at $x = 130r_0$. The dissipation term itself includes the viscous dissipation and the dissipation due to the explicit filtering.

The LES budget is compared in figure 20 with the energy budget obtained by Panchapakesan & Lumley (1993) for a jet at the same Reynolds number

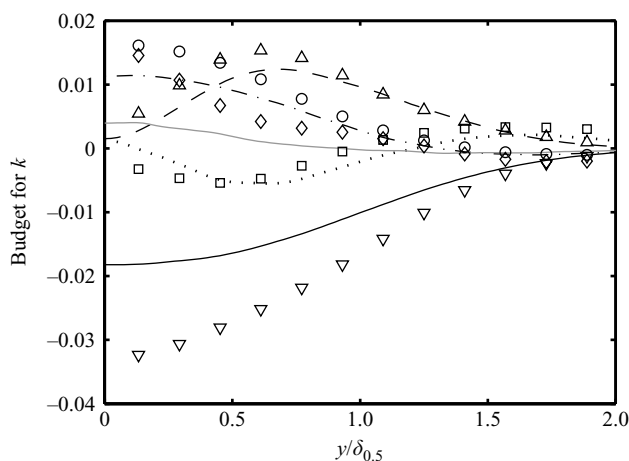


FIGURE 21. Budget for k across the self-similar jet, compared with data of Hussein *et al.* (1994): mean flow convection (---, LES; \circ , Hussein *et al.*), production (— — —, LES; \triangle , Hussein *et al.*), dissipation (——, LES; ∇ , Hussein *et al.*), turbulence diffusion (·····, LES; \square , Hussein *et al.*) and pressure diffusion (— · — · —, LES; \diamond , Hussein *et al.*).

$Re_D = 1.1 \times 10^4$. A very good agreement is displayed for the terms associated with mean flow convection, production, dissipation and turbulence diffusion. This is remarkable, especially since Panchapakesan & Lumley neglected pressure diffusion and predicted dissipation as the balance of the other terms. The Panchapakesan & Lumley hypothesis that the pressure diffusion term can be neglected in the evaluation of the energy budget in a self-similarity jet is thus strengthened, because this term, albeit not negligible, is shown by the simulation to be small with respect to the other energy terms.

The LES results may consequently cast doubt on some assumptions used by Hussein *et al.* (1994) to estimate the energy budget for a jet at a Reynolds number $Re_D = 10^5$ higher than the jet simulated, in which pressure diffusion has been found to be dominant. More precisely, in figure 20, the energy terms that are determined by Hussein *et al.* directly from measurements, namely the mean flow convection, production and turbulence diffusion terms, are roughly similar to the simulation results, whereas the terms which are inferred from turbulence modellings differ significantly. This is the case for the dissipation term, evaluated by Hussein *et al.* using the assumption of axisymmetric turbulence, which is about twice as large as predicted by the simulation, and for the pressure diffusion term, obtained by Hussein *et al.* by difference, which is of the order of mean flow convection whereas this term is small in the LES budget.

In order to clarify the role of the different mechanisms in redistributing the turbulent kinetic energy within the jet, the budgets for the three energy components $[u'u']/2$, $[v'v']/2$ and $[w'w']/2$ are presented in figures 22(a), 22(b) and 22(c). They are compared with the energy component budgets obtained by Panchapakesan & Lumley (1993) by neglecting pressure diffusion, assuming $[w'w'v'] = [v'v'v']$ for the turbulence diffusion, and small-scale isotropy for the dissipation components, and finally evaluating the remaining pressure terms as the balance.

For the three energy components, there is a good collapse between the LES and Panchapakesan & Lumley (1993) terms associated with mean flow convection (black

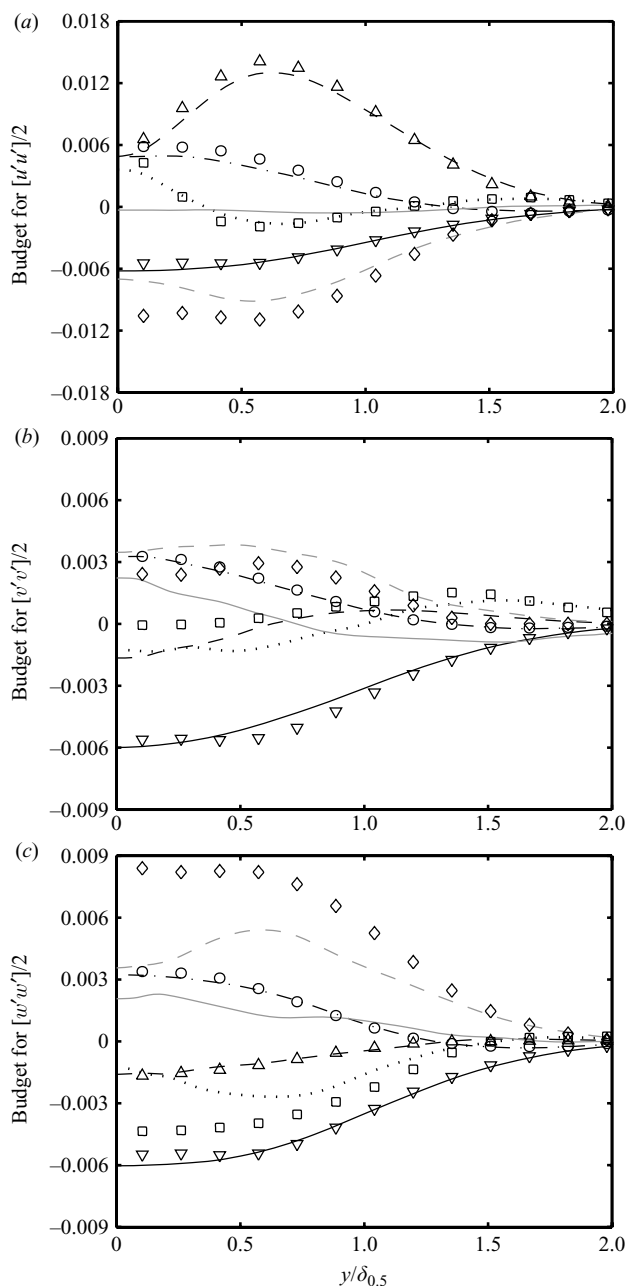


FIGURE 22. Budgets across the self-similar jet for (a) $[u'u']/2$, (b) $[v'v']/2$, (c) $[w'w']/2$: mean flow convection (— · — ·, LES; \circ , Panchapakesan & Lumley (1993)), production (— — —, LES; \triangle , Panchapakesan & Lumley), dissipation (———, LES; ∇ , Panchapakesan & Lumley), turbulence diffusion (·····, LES; \square , Panchapakesan & Lumley), pressure diffusion (———, LES) and pressure-strain correlation term (— — —, LES; \diamond , Panchapakesan & Lumley).

dashed-dotted lines), production (black dashed lines) and dissipation (black solid lines), which supports in particular that the hypothesis of isotropy applies well for the dissipation. As already evidenced by Panchapakesan & Lumley (1993), the turbulent

energy is produced predominantly in the shear zone, and is transferred from the axial component to the radial and azimuthal components mainly by the pressure terms (grey lines).

Regarding turbulence diffusion (black dotted line) and the pressure terms, the agreement between the simulation and Panchapakesan & Lumley (1993) data are satisfactory for the axial component in figure 22(a), but disappointing for the radial and azimuthal components in figures 22(b) and 22(c). For the component $[u'u']/2$, no turbulence modelling, with the exception of the isotropy hypothesis for the dissipation, is involved in the determination of the Panchapakesan & Lumley (1993) energy terms, because turbulence diffusion is calculated explicitly from measurements. For the other two components, Panchapakesan & Lumley (1993) however assumed $[w'w'v'] = [v'v'v']$ for evaluating turbulence diffusion. This results in turbulence diffusion terms near the jet centreline respectively negligible for $[v'v']/2$ and significant for $[w'w']/2$, and, indirectly, in pressure terms with rather low magnitude in figure 22(b) but high magnitude in figure 22(c). The assumption $[w'w'v'] = [v'v'v']$ that is not justified by the LES data in §4.4 thus appears as the main cause for the discrepancies with the simulation results, which exhibit for instance a turbulence diffusion near the jet axis which is noticeable for the radial component, and is not as large as in the Panchapakesan & Lumley (1993) data for the azimuthal component.

It must be pointed out that the pressure diffusion terms (grey solid lines) and the pressure–strain correlation terms (grey dash lines) are computed separately by the simulation. These terms are also represented in figure 23. Pressure diffusion is negligible for the axial energy component, whereas the pressure–strain correlation terms are dominant terms for the three energy components. Moreover, the pressure diffusion terms obtained for the radial and azimuthal components in figure 23(a) have similar amplitudes, the pressure–strain correlation terms displaying the same behaviour in figure 23(b). The transfers of energy by the pressure redistribution terms from the axial component to the radial component and to the azimuthal component are then nearly equal. This is somewhat at variance with the finding of Panchapakesan & Lumley (1993) that the pressure terms are higher for the azimuthal component than for the radial component, which might be due to their estimation of the turbulence diffusion terms discussed above.

The budget computed for the Reynolds stress $[u'v']$ is finally presented in figure 24. The four dominant terms, which are the production, pressure–strain correlation, turbulence diffusion and mean convection terms, compare very well with the experimental data of Panchapakesan & Lumley (1993). The pressure diffusion term is also shown to be small but not negligible.

5. Conclusion

In the present study, turbulence properties and the budgets for the turbulent kinetic energy and for its components have been characterized in the self-similarity region of a round jet at Reynolds number $Re_D = 1.1 \times 10^4$ using an LES combining low-dissipation discretization schemes and an explicit filtering to relax energy through the smaller scales discretized. The flow statistics have been obtained directly from the LES fields, notably without hypothesis on the energy budget terms. Thus they constitute reference solutions which have been systematically compared with the experimental data of Panchapakesan & Lumley (1993) for a jet at the same Reynolds number.

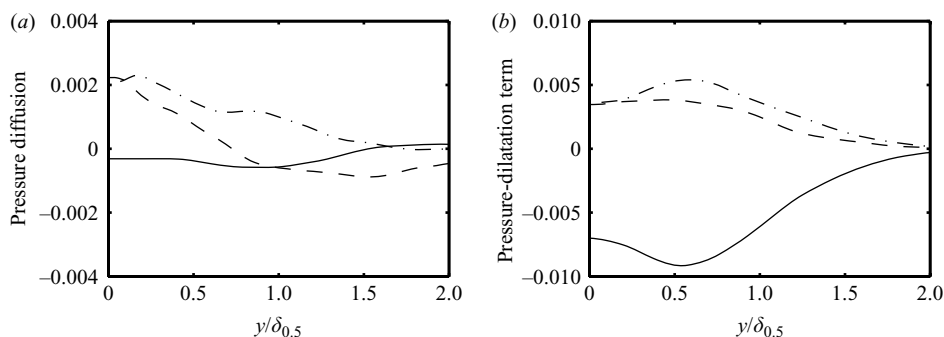


FIGURE 23. Profiles across the self-similar jet of (a) the pressure diffusion terms and (b) the pressure-strain correlation terms in the budgets for —, $[u'u']/2$; — —, $[v'v']/2$; — · —, $[w'w']/2$.

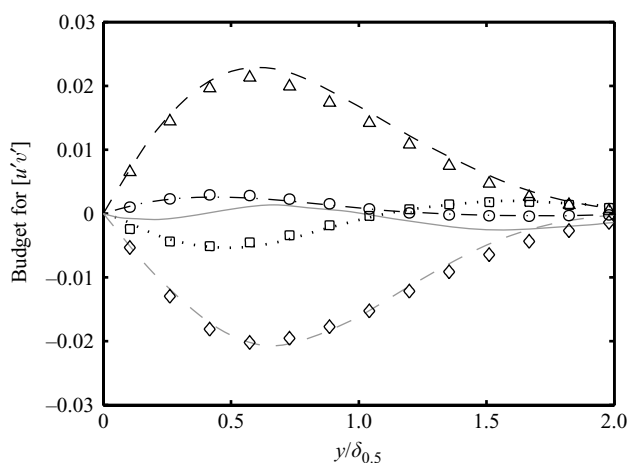


FIGURE 24. Budget across the self-similar jet for $[u'v']$: mean flow convection (— · — ·, LES; \circ , Panchapakesan & Lumley (1993)), production (— — —, LES; \triangle , Panchapakesan & Lumley), dissipation (——, LES; ∇ , Panchapakesan & Lumley), turbulence diffusion (·····, LES; \square , Panchapakesan & Lumley), pressure diffusion (——, LES) and pressure-strain correlation term (— — —, LES; \diamond , Panchapakesan & Lumley).

Good agreement is generally found both for the self-similarity establishment and for the radial profiles across the self-similar jet.

The validity of the LES approach is strengthened by the results obtained for the present jet, but also by the fact that the energy dissipation due to the explicit filtering is evaluated directly in the turbulent kinetic energy budget derived from the filtered compressible Navier–Stokes equations. The sum of the energy terms has been checked to be nearly zero, which supports the relevance of the energy equation including the filtering dissipation, and indicates that there is negligible spurious numerical dissipation. The filtering activity has then been examined from the variations of the filtering dissipation and of the viscous dissipation within the jet. It has been shown

in particular to adjust itself to the grid spacing, to the flow development and to the turbulence anisotropy.

In the present jet, the third-order moments of the azimuthal velocity and the pressure–velocity correlations, which have been obtained in the self-preserving jets of Wygnanski & Fiedler (1969), Panchapakesan & Lumley (1993) and Hussein *et al.* (1994) using turbulence considerations, have been predicted directly by the LES. The justification of the assumptions made by these authors has thus been discussed. The LES has for instance shown that the approximation $[w'w'v'] = [v'v'v']$ used by Panchapakesan & Lumley and Hussein *et al.* is very rough, and that the pressure–velocity correlations can be estimated fairly well from third-order velocity moments. Turbulence diffusion has also been found to be small in the budget for the turbulent kinetic energy, which is in agreement with an hypothesis of Panchapakesan & Lumley, but may cast doubt on the dissipation and turbulence diffusion terms evaluated in the energy budget of Hussein *et al.* In the same way, the redistribution of turbulent energy between the velocity components has been clarified by the LES budgets, which has permitted to lift some uncertainties associated with the approximations made in the experiments. The roles of the pressure diffusion and of the pressure–strain correlation terms have also been quantified separately. These terms associated with pressure appear to transfer turbulent energy from the axial velocity component to the radial component and to the azimuthal component in similar proportions.

Finally, the present LES has been computationally expensive, but provides reference solutions for further studies. Future simulations could for instance be performed in order to study the influence of the discretization, of the inflow conditions and of the Reynolds number of the jets on the properties of the self-similarity flow region. These issues are indeed still matters of debate. It will be also interesting to apply the present LES method to other flow configurations because it appears as an appropriate tool for investigating the quality of simulations, as well as physical mechanisms encountered in practical flows.

The authors gratefully acknowledge the *Institut du Développement et des Ressources en Informatique Scientifique* (IDRIS) of the CNRS and the *Centre de Calcul Recherche et Technologie* of the CEA (the French Atomic Energy Agency) for providing CPU time on Nec computers and technical assistance.

Appendix. Derivation of the equations for the budgets of the turbulent kinetic energy

The developments of the energy budget equations in compressible LES involving explicit filtering of the flow variables are presented in detail in this appendix. The budget equations are determined from the following equations,

$$\frac{\partial \bar{\rho}}{\partial t} + \frac{\partial \bar{\rho} \tilde{u}_j}{\partial x_j} = D_{sf}(\bar{\rho}), \quad (5.1)$$

$$\frac{\partial \bar{\rho} \tilde{u}_i}{\partial t} + \frac{\partial \bar{\rho} \tilde{u}_i \tilde{u}_j}{\partial x_j} = -\frac{\partial \bar{p}}{\partial x_i} + \frac{\partial \tilde{\tau}_{ij}}{\partial x_j} + \frac{\partial T_{ij}}{\partial x_j} + D_{sf}(\bar{\rho} u_i), \quad (5.2)$$

which are the LES equations (2.1) and (2.2) including the operators D_{sf} associated with the filterings of the density and of the momentum variables (see expressions (2.5) and (2.8)), where the SGS term \mathcal{R}_i is removed.

In what follows, statistical averaging is denoted by $\langle \cdot \rangle$ and Favre averaging by $[\cdot]$, yielding $[u_i] = \langle \bar{\rho} \tilde{u}_i \rangle / \langle \bar{\rho} \rangle$. The fluctuating velocity is then defined by $u'_i = \tilde{u}_i - [u_i]$, and the turbulent kinetic energy by $\langle \bar{\rho} \rangle k = \langle \bar{\rho} u_i'^2 \rangle / 2$. Equation (5.2) is first written in the non-conservative form

$$\underbrace{\tilde{u}_i \left(\frac{\partial \bar{\rho}}{\partial t} + \frac{\partial \bar{\rho} \tilde{u}_j}{\partial x_j} \right)}_{=D_{sf}(\bar{\rho})} + \bar{\rho} \frac{\partial \tilde{u}_i}{\partial t} + \bar{\rho} \tilde{u}_j \frac{\partial \tilde{u}_i}{\partial x_j} = -\frac{\partial \bar{p}}{\partial x_i} + \frac{\partial \tilde{\tau}_{ij}}{\partial x_j} + \frac{\partial T_{ij}}{\partial x_j} + D_{sf}(\bar{\rho} \tilde{u}_i), \quad (5.3)$$

and multiplied by u'_i . Then it follows that

$$\underbrace{\bar{\rho} u'_i \frac{\partial \tilde{u}_i}{\partial t}}_A + \underbrace{\bar{\rho} u'_i \tilde{u}_j \frac{\partial \tilde{u}_i}{\partial x_j}}_B = \underbrace{-u'_i \frac{\partial \bar{p}}{\partial x_i}}_C + \underbrace{u'_i \frac{\partial \tilde{\tau}_{ij}}{\partial x_j}}_D + \underbrace{u'_i \frac{\partial T_{ij}}{\partial x_j}}_E + u'_i D_{sf}(\bar{\rho} \tilde{u}_i) - u'_i \tilde{u}_i D_{sf}(\bar{\rho}). \quad (5.4)$$

Term A in (5.4) is decomposed as

$$A = \bar{\rho} u'_i \frac{\partial [u_i]}{\partial t} + \bar{\rho} u'_i \frac{\partial u'_i}{\partial t}, \quad (5.5)$$

$$= \bar{\rho} u'_i \frac{\partial [u_i]}{\partial t} + \bar{\rho} \frac{\partial}{\partial t} \left(\frac{u_i'^2}{2} \right), \quad (5.6)$$

$$= \bar{\rho} u'_i \frac{\partial [u_i]}{\partial t} + \frac{\partial}{\partial t} \left(\frac{1}{2} \bar{\rho} u_i'^2 \right) - \frac{u_i'^2}{2} \frac{\partial \bar{\rho}}{\partial t}, \quad (5.7)$$

and averaged, giving

$$\langle A \rangle = - \left\langle \frac{u_i'^2}{2} \frac{\partial \bar{\rho}}{\partial t} \right\rangle. \quad (5.8)$$

Term B in (5.4) becomes

$$B = \bar{\rho} u'_i [u_j] \frac{\partial [u_i]}{\partial x_j} + \bar{\rho} u'_i u'_j \frac{\partial [u_i]}{\partial x_j} + \bar{\rho} u'_i \tilde{u}_j \frac{\partial u'_i}{\partial x_j}, \quad (5.9)$$

with

$$\bar{\rho} u'_i \tilde{u}_j \frac{\partial u'_i}{\partial x_j} = \bar{\rho} \tilde{u}_j \frac{\partial}{\partial x_j} \left(\frac{u_i'^2}{2} \right), \quad (5.10)$$

$$= \frac{\partial}{\partial x_j} \left(\bar{\rho} \tilde{u}_j \frac{u_i'^2}{2} \right) - \frac{u_i'^2}{2} \frac{\partial \bar{\rho} \tilde{u}_j}{\partial x_j}, \quad (5.11)$$

$$= \frac{\partial}{\partial x_j} \left(\bar{\rho} [u_j] \frac{u_i'^2}{2} \right) + \frac{\partial}{\partial x_j} \left(\bar{\rho} u'_j \frac{u_i'^2}{2} \right) - \frac{u_i'^2}{2} \frac{\partial \bar{\rho} \tilde{u}_j}{\partial x_j}, \quad (5.12)$$

and one gets after statistical averaging

$$\langle B \rangle = \langle \bar{\rho} u'_i u'_j \rangle \frac{\partial [u_i]}{\partial x_j} + \frac{\partial}{\partial x_j} \left(\left\langle \bar{\rho} \frac{u_i'^2}{2} \right\rangle [u_j] \right) + \frac{\partial}{\partial x_j} \left\langle \bar{\rho} u'_j \frac{u_i'^2}{2} \right\rangle - \left\langle \frac{u_i'^2}{2} \frac{\partial \bar{\rho} \tilde{u}_j}{\partial x_j} \right\rangle. \quad (5.13)$$

The sum of expressions (5.8) and (5.13) yields

$$\begin{aligned} \langle A \rangle + \langle B \rangle = & \frac{\partial}{\partial x_j} \left(\left\langle \frac{1}{2} \bar{\rho} u_i^2 \right\rangle [u_j] \right) + \langle \bar{\rho} u'_i u'_j \rangle \frac{\partial [u_i]}{\partial x_j} \\ & + \frac{1}{2} \frac{\partial}{\partial x_j} \langle \bar{\rho} u_i^2 u'_j \rangle - \left\langle \frac{u_i^2}{2} \left(\frac{\partial \bar{\rho}}{\partial t} + \frac{\partial \bar{\rho} \tilde{u}_j}{\partial x_j} \right) \right\rangle. \end{aligned} \quad (5.14)$$

$= D_{sf}(\bar{\rho})$

Using averaging, the term C involving pressure in (5.4) provides

$$\begin{aligned} \langle C \rangle = & - \langle u'_i \rangle \frac{\partial \langle \bar{p} \rangle}{\partial x_i} - \left\langle u'_i \frac{\partial p'}{\partial x_i} \right\rangle \\ = & - \langle u'_i \rangle \frac{\partial \langle \bar{p} \rangle}{\partial x_i} - \frac{\partial}{\partial x_i} \langle p' u'_i \rangle + \left\langle p' \frac{\partial u'_i}{\partial x_i} \right\rangle, \end{aligned} \quad (5.15)$$

where the fluctuating pressure is $p' = p - \langle \bar{p} \rangle$. The terms $\langle D \rangle$ and $\langle E \rangle$ involving the viscous and the subgrid stress tensors are also written as

$$\langle D \rangle = \frac{\partial}{\partial x_j} \langle u'_i \tilde{\tau}_{ij} \rangle - \left\langle \tilde{\tau}_{ij} \frac{\partial u'_i}{\partial x_j} \right\rangle, \quad (5.16)$$

$$\langle E \rangle = \frac{\partial}{\partial x_j} \langle u'_i T_{ij} \rangle - \left\langle T_{ij} \frac{\partial u'_i}{\partial x_j} \right\rangle. \quad (5.17)$$

The budgets for the three components of the turbulent kinetic energy are finally obtained by averaging (5.4):

$$\begin{aligned} 0 = & - \frac{\partial}{\partial x_j} \left(\frac{1}{2} \langle \bar{\rho} u_i^2 \rangle [u_j] \right) - \langle \bar{\rho} u'_i u'_j \rangle \frac{\partial [u_i]}{\partial x_j} - \frac{1}{2} \frac{\partial}{\partial x_j} \langle \bar{\rho} u_i^2 u'_j \rangle \\ & - \frac{\partial}{\partial x_i} \langle p' u'_i \rangle + \left\langle p' \frac{\partial u'_i}{\partial x_i} \right\rangle - \langle u'_i \rangle \frac{\partial \langle \bar{p} \rangle}{\partial x_i} \\ & - \left\langle \tilde{\tau}_{ij} \frac{\partial u'_i}{\partial x_j} \right\rangle - \left\langle T_{ij} \frac{\partial u'_i}{\partial x_j} \right\rangle + \frac{\partial}{\partial x_j} \langle u'_i \tilde{\tau}_{ij} \rangle + \frac{\partial}{\partial x_j} \langle u'_i T_{ij} \rangle \\ & + \langle u'_i D_{sf}(\bar{\rho} u_i) \rangle - \langle u'_i \tilde{u}_i D_{sf}(\bar{\rho}) \rangle + \frac{1}{2} \langle u_i^2 D_{sf}(\bar{\rho}) \rangle. \end{aligned} \quad (5.18)$$

Similar developments can be performed from (5.1) and (5.2) to derive the budget equations for the Reynolds stresses. The equation for the stress component $[u'_1 u'_2] = \langle \bar{\rho} u'_1 u'_2 \rangle / \langle \bar{\rho} \rangle$ is for instance given by

$$\begin{aligned} 0 = & - \frac{\partial}{\partial x_j} (\langle \bar{\rho} u'_1 u'_2 \rangle [u_j]) - \langle \bar{\rho} u'_1 u'_j \rangle \frac{\partial [u_1]}{\partial x_j} - \langle \bar{\rho} u'_1 u'_j \rangle \frac{\partial [u_2]}{\partial x_j} \\ & - \frac{\partial}{\partial x_j} \langle \bar{\rho} u'_1 u'_2 u'_j \rangle - \frac{\partial}{\partial x_1} \langle p' u'_2 \rangle - \frac{\partial}{\partial x_2} \langle p' u'_1 \rangle + \left\langle p' \frac{\partial u'_2}{\partial x_1} \right\rangle \\ & + \left\langle p' \frac{\partial u'_1}{\partial x_2} \right\rangle - \langle u'_2 \rangle \frac{\partial \langle p \rangle}{\partial x_1} - \langle u'_1 \rangle \frac{\partial \langle p \rangle}{\partial x_2} - \left\langle \tilde{\tau}_{1j} \frac{\partial u'_2}{\partial x_j} \right\rangle - \left\langle \tilde{\tau}_{2j} \frac{\partial u'_1}{\partial x_j} \right\rangle \end{aligned}$$

$$\begin{aligned}
& + \frac{\partial}{\partial x_j} \langle u'_2 \tilde{\tau}_{1j} \rangle + \frac{\partial}{\partial x_j} \langle u'_1 \tilde{\tau}_{2j} \rangle - \left\langle \tau_{1j} \frac{\partial u'_2}{\partial x_j} \right\rangle - \left\langle \tau_{2j} \frac{\partial u'_1}{\partial x_j} \right\rangle \\
& + \frac{\partial}{\partial x_j} \langle u'_2 \tau_{1j} \rangle + \frac{\partial}{\partial x_j} \langle u'_1 \tau_{2j} \rangle + \langle u'_2 D_{sf}(\overline{\rho u_1}) \rangle + \langle u'_1 D_{sf}(\overline{\rho u_2}) \rangle \\
& - \langle u'_2 \tilde{u}_1 D_{sf}(\overline{\rho}) \rangle - \langle u'_1 \tilde{u}_2 D_{sf}(\overline{\rho}) \rangle + \langle u'_1 u'_2 D_{sf}(\overline{\rho}) \rangle.
\end{aligned} \tag{5.19}$$

REFERENCES

- BERLAND, J., BOGEY, C. & BAILLY, C. 2007 Numerical study of screech generation in a planar supersonic jet. *Phys. Fluids* **19** (7), 075105.
- BOERSMA, B. J., BRETHOUWER, G. & NIEUWSTADT, F. T. M. 1998 A numerical investigation on the effect of the inflow conditions on the self-similar region of a round jet. *Phys. Fluids* **10** (4), 899–909.
- BOGEY, C. & BAILLY, C. 2002 Three-dimensional non-reflective boundary conditions for acoustic simulations: far field formulation and validation test cases. *Acta Acust.* **88** (4), 463–471.
- BOGEY, C. & BAILLY, C. 2004 A family of low dispersive and low dissipative explicit schemes for flow and noise computations. *J. Comput. Phys.* **194** (1), 194–214.
- BOGEY, C. & BAILLY, C. 2005a Decrease of the effective Reynolds number with eddy-viscosity subgrid-scale modeling. *AIAA J.* **43** (2), 437–439.
- BOGEY, C. & BAILLY, C. 2005b Effects of inflow conditions and forcing on a Mach 0.9 jet and its radiated noise. *AIAA J.* **43** (5), 1000–1007.
- BOGEY, C. & BAILLY, C. 2006a Investigation of downstream and sideline subsonic jet noise using Large Eddy Simulation. *Theor. Comput. Fluid Dyn.* **20** (1), 23–40.
- BOGEY, C. & BAILLY, C. 2006b Large Eddy Simulations of round free jets using explicit filtering with/without dynamic Smagorinsky model. *Intl J. Heat Fluid Flow* **27** (4), 603–610.
- BOGEY, C. & BAILLY, C. 2006c Large Eddy Simulations of transitional round jets: influence of the Reynolds number on flow development and energy dissipation. *Phys. Fluids* **18** (6), 065101.
- BOGEY, C. & BAILLY, C. 2006d Computation of a high Reynolds number jet and its radiated noise using large eddy simulation based on explicit filtering. *Comput. Fluids* **35** (10), 1344–1358.
- BOGEY, C. & BAILLY, C. 2007 An analysis of the correlations between the turbulent flow and the sound pressure field of subsonic jets. *J. Fluid Mech.* **583**, 71–97.
- BOGEY, C., BAILLY, C. & JUVÉ, D. 2003 Noise investigation of a high subsonic, moderate Reynolds number jet using a compressible LES. *Theor. Comput. Fluid Dyn.* **16** (4), 273–297.
- BRADBURY, L. J. S. 1965 The structure of a self-preserving turbulent plane jet. *J. Fluid Mech.* **23** (1), 31–64.
- BURATTINI, P., ANTONIA, R. A. & DANAILA, L. 2005 Similarity in the far field of a turbulent round jet. *Phys. Fluids* **17** (2), 025101.
- DANTINNE, G., JEANMART, H., WINCKELMANS, G. S., LEGAT, V. & CARATI, D. 1998 Hyperviscosity and vorticity-based models for subgrid scale modeling. *Appl. Sci. Res.* **59**, 409–420.
- DAVIES, P. O. A. L., FISHER, M. J. & BARRATT, M. J. 1962 The characteristics of the turbulence in the mixing region of a round jet. *J. Fluid Mech.* **15**, 337–367.
- DEJOAN, A. & LESCHZNER, M. A. 2005 Large eddy simulation of a plane turbulent wall jet. *Phys. Fluids A* **17** (2), 025102.
- DEO, R. C., MI, J. & NATHAN, G. J. (2008) The influence of Reynolds number on a plane jet. *Phys. Fluids* **20**, 075108.
- DOMARADZKI, J. A. & ADAMS, N. A. 2002 Direct modeling of subgrid scales of turbulence in Large-Eddy Simulation. *J. Turbul.* **3**, 1–19.
- DOMARADZKI, J. A., XIAO, Z. & SMOLARKIEWICZ, P. K. 2003 Effective eddy viscosities in implicit large eddy simulations of turbulent flows. *Phys. Fluids* **15** (12), 3890–3893.
- DOMARADZKI, J. A. & YEE, P. P. 2000 The subgrid-scale estimation model for high Reynolds number turbulence. *Phys. Fluids* **12** (1), 193–196.

- GARNIER, E., MOSSI, M., SAGAUT, P., COMTE, P. & DEVILLE, M. 1999 On the use of shock-capturing schemes for large-eddy simulation. *J. Comput. Phys.* **153** (2), 273–311.
- GEORGE, W. K. & HUSSEIN, H. J. 1991 Locally axisymmetric turbulence. *J. Fluid Mech.* **233**, 1–23.
- GEURTS, B. J. 2004 *Elements of Direct and Large-Eddy Simulation*. Edwards.
- GEURTS, B. J. & FRÖHLICH, J. 2002 A framework for predicting accuracy limitations in large-eddy simulations. *Phys. Fluids* **14** (6), 41–44.
- GRINSTEIN, F. F. & FUREBY, C. 2002 Recent progress on MILES for high Reynolds number flows. *J. Fluid Engng* **124**, 848–861.
- GUTMARK, E. & WYGNANSKI, I. 1976 The planar turbulent jet. *J. Fluid Mech.* **73**, 465–495.
- HICKEL, S., ADAMS, N. A. & DOMARADZKI, J. A. 2006 An adaptative local deconvolution method for implicit LES. *J. Comput. Phys.* **213** (2), 413–436.
- HUSSEIN, H. J., CAPP, S. P. & GEORGE, W. K. 1994 Velocity measurements in a high-Reynolds-number, momentum-conserving, axisymmetric, turbulent jet. *J. Fluid Mech.* **258**, 31–75.
- LE RIBAUT, C., SARKAR, S. & STANLEY, S. 1999 Large eddy simulation of a plane jet. *Phys. Fluids* **11** (10), 3069–3083.
- LESIEUR, M. & MÉTAIS, O. 1996 New trends in large-eddy simulations of turbulence. *Annu. Rev. Fluid Mech.* **28**, 45–82.
- LUMLEY, J. L. 1978 Computational modelling of turbulent flows. *Adv. Appl. Mech.* **18**, 123–126.
- MANSOUR, N. N., KIM, J. & MOIN, P. 1988 Reynolds-stress and dissipation-rate budgets in a turbulent channel flow. *J. Fluid Mech.* **194**, 15–44.
- MARSDEN, O., BOGEY, C. & BAILLY, C. 2008 Direct noise computation of the turbulent flow around a zero-incidence airfoil. *AIAA J.* **46** (4), 874–883.
- MATHEW, J., LECHNER, R., FOYSI, H., SESTERHENN, J. & FRIEDRICH, R. 2003 An explicit filtering method for large eddy simulation of compressible flows. *Phys. Fluids* **15** (8), 2279–2289.
- MENEVEAU, C. & KATZ, J. 2000 Scale-invariance and turbulence models for large-eddy simulation. *Annu. Rev. Fluid Mech.* **32**, 1–32.
- PANCHAPAKESAN, N. R. & LUMLEY, J. L. 1993 Turbulence measurements in axisymmetric jets of air and helium. Part I. Air jet. *J. Fluid Mech.* **246**, 197–223.
- PASQUETTI, R. 2006 Spectral vanishing viscosity method for large eddy simulation of turbulent flows. *J. Sci. Comput.* **27**, 365–375.
- POPE, S. B. 2000 *Turbulent Flows*. Cambridge University Press.
- RICOU, F. P. & SPALDING, D. B. 1961 Measurements of entrainment by axisymmetrical turbulent jets. *J. Fluid Mech.* **11**, 21–32.
- RIZZETTA, D. P., VISBAL, M. R. & BLAISDELL, G. A. 2003 A time-implicit high-order compact differencing and filtering scheme for large-eddy simulation. *Intl J. Num. Methods Fluids* **42** (6), 665–693.
- SAGAUT, P. 2005 *Large-Eddy Simulation for Incompressible Flows: An Introduction*, 3rd ed. Springer.
- SAMI, S. 1967 Balance of turbulence energy in the region of jet-flow establishment. *J. Fluid Mech.* **29** (1), 81–92.
- SAMI, S., CARMODY, T. & ROUSE, H. 1967 Jet diffusion in the region of flow establishment. *J. Fluid Mech.* **27** (2), 231–252.
- SCHLATTER, P., STOLZ, S. & KLEISER, L. 2004 LES of transitional flows using the approximate deconvolution model. *Intl J. Heat Fluid Flow* **25** (3), 549–558.
- SCHLATTER, P., STOLZ, S. & KLEISER, L. 2006 Analysis of the SGS energy budget for deconvolution- and relaxation-based models in channel flow. In *Direct and Large-Eddy Simulation VI* (ed. E. Lamballais, R. Friedrich, B. J. Geurts & O. Métais), pp. 135–142. Springer.
- STANLEY, S. A., SARKAR, S. & MELLADO, J. P. 2002 A study of the flowfield evolution and mixing in a planar turbulent jet using direct numerical simulation. *J. Fluid Mech.* **450**, 377–407.
- STOLZ, S., ADAMS, N. A. & KLEISER, L. 2001 An approximate deconvolution model for Large-Eddy Simulation of incompressible flows. *Phys. Fluids* **13** (4), 997–1015.
- TAM, C. K. W. & WEBB, J. C. 1993 Dispersion-relation-preserving finite difference schemes for computational acoustics. *J. Comput. Phys.* **107** (2), 262–281.

- UDDIN, M. & POLLARD, A. 2007 Self-similarity of coflowing jets: the virtual origin. *Phys. Fluids* **19**, 068103-1–068103-4.
- VREMAN, B., GEURTS, B. & KUERTEN, H. 1995 Subgrid-modeling in LES of compressible flow. *Appl. Sci. Res.* **54**, 191–203.
- VREMAN, B., GEURTS, B. & KUERTEN, H. 1997 Large-eddy simulation of the turbulent mixing layer. *J. Fluid Mech.* **339**, 357–390.
- WEISGRABER, T. H. & LIEPMANN, D. 1998 Turbulent structure during transition to self-similarity in a round jet. *Exp. Fluids* **24**, 210–224.
- WYGNANSKI, I. & FIEDLER, H. 1969 Some measurements in the self-preserving jet. *J. Fluid Mech.* **38** (3), 577–612.